Received: 26 March 2024 | Revised: 28 August 2024 | Accepted: 1 September 2024

DOI: 10.1002/esp.5996

CASE STUDY

ESPL WILEY

Tsunami propagation and flooding maps: An application for the Island of Lampedusa, Sicily Channel, Italy

Laura Borzì[1] | Pietro Scala[2] | Salvatore Distefano[1] | F. X. Anjar Tri Laksono[3,4] | Giorgio Manno[2] | Sara Innangi[5] | Fabiano Gamberi[6] | János Kovács[3] | Giuseppe Ciraolo[2] | Agata Di Stefano[1]

[1]Dipartimento di Scienze Biologiche, Geologiche ed Ambientali, Università Degli Studi di Catania, Corso Italia, Catania, Italy

[2]Department of Engineering (DI), University of Palermo, Viale delle Scienze, Palermo, Italy

[3]Doctoral School of Earth Sciences, Department of Geology and Meteorology, Institute of Geography and Earth Sciences, Faculty of Sciences, University of Pécs, Pécs, Hungary

[4]Department of Geological Engineering, Faculty of Engineering, Jenderal Soedirman University, Purwokerto, Indonesia

[5]Istituto per l'Ambiente Marino Costiero of CNR, Naples, Italy

[6]Istituto di Scienze Marine Consiglio Nazionale delle Ricerche, Bologna, Italy

Correspondence
Pietro Scala, Department of Engineering (DI), University of Palermo, Viale delle Scienze, Bd. 8, 90128 Palermo, Italy.
Email: pietro.scala@unipa.it

Funding information
European Union, Grant/Award Number: PE0000005

Abstract

The Mediterranean coastlines are densely populated zones which host key socio-economic and commercial activities. For this reason, coastal areas are vulnerable sites in case of natural disasters as tsunamis that can strike coasts causing widespread damage to the population and facilities. For these reasons, several studies were performed over the last decade to study the impact of tsunami waves on the coasts. This research assessed the inundation risk due to a tsunami wave which can hit the south-eastern coast of Lampedusa Island. The coastal low-lying geomorphological setting of the southeastern part of the island led to significant socio-economic growth, but Lampedusa falls within the Mediterranean Sea, a high-tsunamigenic area, therefore, the need to investigate tsunami propagation and coastal flooding of this sensitive site emerged. For this scope, a calculation chain model was implemented incorporating three steps: the DELFT-3D software for earthquake effects modelling, MIKE 21 Flow Model FM for nearshore propagation and HEC-RAS for onshore tsunami inundation modelling. The simulations illustrate the impact of three tsunami scenarios with different magnitudes (M_w 8.5, 7.5, 6.5) generated by hypothetical earthquakes in the Hellenic Arc. In the M_w 8.5 magnitude scenario, significant flooding occurs in the harbour region, with maximum water depths reaching approximately 3.5 m. The maximum water velocity in this scenario reaches about 15 m/s in the eastern portion, adjacent to cliffs impacted by the tsunami wave. In contrast, the M_w 7.5 magnitude scenario demonstrates reduced flooded areas, with the cliffs containing the waves and preventing further flooding. Water depths and velocities in the M_w 7.5 scenario remain minimal. Changes in both propagation and flooding are not significant between scenarios M_w 7.5 and M_w 6.5. This methodology can be employed for more accurate tsunami wave simulations not only in the Mediterranean region but also in various case studies.

KEYWORDS
coastal flooding, Lampedusa Island, numerical modelling, tsunami propagation

1 | INTRODUCTION

As well as representing the site of complex interactions between marine and continental processes (Distefano et al., 2021a, 2021b; Laksono et al., 2022, 2023; Swift, 1968), coastal zones provide space for living and working for a large part of the world's population, and they host most of the world's megacities. These areas can be exposed to catastrophic coastal flooding caused by

various phenomena: tsunamis, hurricanes, storm surges and river floods (Kron, 2013). Tsunamis can be generated by earthquakes, coastal landslides, submerged landslides and collapsing seamounts. Historically, both earthquakes and volcanic eruptions have been the main sources of tsunamis in the Mediterranean region (Heidarzadeh, Gusman, & Mulia, 2023; Soloviev, 1990; Tinti & Maramai, 1996), which represents – in contrast to oceanic areas – a relatively small environment characterized by densely populated coastal areas (Álvarez-Gómez et al., 2011). For these reasons, the Mediterranean coast is a suitable test site for the study of the impact of tsunamis.

The Mediterranean area is characterized by a complex geodynamic framework related to the tectonically active convergence between the Eurasian and Nubian plates and the differential subduction rates of ~5–10 mm/yr across the subduction boundaries of the Hellenic and Calabrian arcs (Masina et al., 2017; Royden & Papanikolaou, 2011). This area is therefore be affected by significant seismic activity, both in terms of frequency and intensity (e.g. Altinok et al., 2011; Maramai, Brizuela, & Graziani, 2014; G. Papadopoulos et al., 2007; Salamon et al., 2011; Soloviev et al., 2000; Tinti, Maramai, & Graziani, 2004; Triantafyllou et al., 2024).

According to the Euro-Mediterranean Tsunami Catalogue (Maramai, Brizuela, & Graziani, 2014), several tsunami events have occurred in the eastern Mediterranean Sea, including for example July 21, AD 365 and August 8, 1303 in Crete; May 3, AD 1481 in Rhodes; February 28, AD 1629 in Kythera; and January 22, AD 1899 in Kyparissia (England et al., 2015; Pararas-Carayannis, 2011; Yolsal-Çevikbilen & Taymaz, 2012). The estimated magnitudes of historically documented tsunamigenic earthquakes in the eastern Mediterranean region and its adjacent seas, over the past 2.5 millennia, range from Mw 6.5 to approximately Mw 8.5 (Masina et al., 2017; Papadopoulos & Papageorgiou, 2014).

In the scientific literature, there are several studies on past tsunamis recorded in the Mediterranean Sea. These studies analysed and, in some cases, pointed out the possible tsunami sources and effects on the coasts (e.g. Menager, Guilhem Trilla, & Delouis, 2023; Papadopoulos & Fokaefs, 2005). However, in recent years, there has been a limited effort in the scientific community to model tsunami dynamics, from its propagation from the triggering source to the impact and effects of tsunami waves on the coasts. There are a few manuscripts that examine the relationship between the seismic origin, the tsunami propagation and the coastal flooding (e.g. Álvarez-Gómez, Herrero-Barbero, & Martínez-Díaz, 2023; Heinrich et al., 2024; Lo Re et al., 2022; Lo Re, Manno, & Ciraolo, 2020; Peresan & Hassan, 2024) and less numerous studies can be found (Mueller et al., 2020) that analysed the impact of possible tsunamigenic events in the central Mediterranean area by simulating real seismic tsunami events, even though there are densely populated islands with different geological characteristics, as the Maltese archipelago, Pantelleria and the Pelagie Islands, which share a poorly protected position from possible catastrophic tsunami waves generated by the tectonic sources of the eastern Mediterranean.

This study aims to assess the coastal inundation of Lampedusa Island, due to a tsunami. To obtain this result, seismic scenarios with different magnitudes and different physical parameters of the fault were considered on the Hellenic Arc. The propagation of a tsunami from the Hellenic Arc to the island of Lampedusa was then carried out. A properly implemented computational chain was used for the numerical simulation.

Three numerical models were used respectively, the first to propagate the tsunami from the eastern to the central Mediterranean area, the second to propagate the tsunami from offshore to the southeastern coast of Lampedusa Island, and finally the third model to assess the tsunami inundation. Lampedusa Island is a highly attractive place for tourism and offers several beaches of rare beauty and natural and landscape value, which make the Island one of the most popular destinations in the Mediterranean Sea, and the low-lying coastal setting of the southeastern part of the island provides an ideal location for transport infrastructures and commercial facilities. Indeed, this area was chosen because the risk of a potential tsunami disaster inundation could be rather high.

2 | STUDY AREA

2.1 | Geodynamic framework of the central Mediterranean Sea

Three geodynamic regions where the structural sources are responsible for the major earthquake hazard in the central Mediterranean region are as follows (Figure 1):

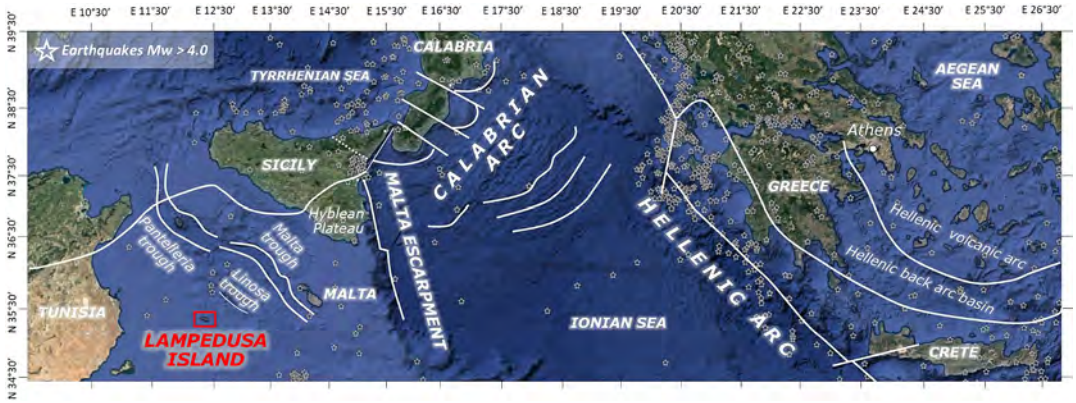

FIGURE 1 Morphotectonic schematic map of the Central Mediterranean Sea (Finetti et al., 2005), showing the location of the recent earthquakes (1985–2023, INGV catalogue) with mw > 4.0. The maximum concentration earthquakes are along the tectonic structures of the Hellenic Arc (Lo Re, Manno, & Ciraolo, 2020).

1. The northern segment of the Malta Escarpment is characterized by NNW–SSE, east-dipping extensional faults and a lithospheric-scale lateral slab tear between the Ionian oceanic basin and the Hyblean Plateau (Polonia, Vaiani, & De Lange, 2016). These active faults are mechanically capable of generating M_w 6–7 earthquakes and may be responsible for some enigmatic historical earthquakes (Mueller et al., 2020).
2. The Calabrian Arc has been characterized by the subduction of remnants of the Mesozoic Tethys Ocean for the last 80 Ma (Faccenna et al., 2001; Mueller et al., 2020). Subduction today is confined to a 150 km zone between the Strait of Messina and Catanzaro (South Italy) and is associated with slab roll-back that began in the late Miocene (Goes et al., 2004). Large historical earthquakes, such as the 1,693 earthquake (Mw 7.3) in south-eastern Sicily (Gutscher et al., 2006) and the 1905 earthquake (M_w 7.0) in central Calabria have been associated with the shallow portion of the plate interface or slab.
3. The Hellenic Arc and its back-arc region of the Aegean Sea are the most seismically active regions in the Mediterranean (Heidarzadeh & Gusman, 2021; Papazachos, 1996). As a result of the stress build-up along the boundaries and within the affected crustal blocks, shallow, interpolate and intermediate-depth seismicity is extremely high (365 A.D. earthquake – M_w 8.4) in the western segment of the Hellenic Arc; 1,303 A. D, earthquake (M_w 8.0), in the eastern segment of the Hellenic Arc; 1956 earthquake (M_w 7.5) in the south Aegean Sea (Mueller et al., 2020).

In Figure 1 all the earthquakes (Mw > 4) from the INGV catalogue (1985–2023 - http://terremoti.ingv.it/en), the EMSC catalogue (2004–2023 - https://www.emsc-csem.org/Earthquake/?filter=yes) and the EMEC catalogue (1900–2006 - http://emec.gfz-potsdam.de/pub/EMEC_Online/emec_online_frame_map.html) are projected. Most of these earthquakes occur along the Hellenic Arc, which extends for hundreds of kilometres NW-SE. The extensive tectonic lineaments and high frequency of seismogenic events along the Hellenic make this site a main source for modelling Mediterranean tsunamis that pose a threat to vulnerable coastal regions, including Lampedusa Island.

2.2 | Geomorphological setting of the Lampedusa Island

The Lampedusa Island (Sicily, Italy) is located in the southern Mediterranean, at halfway between Sicily and Libya (35°30′13″N–12°36′25″E), about 250 km southwest of the Sicilian coasts and 130 km east of those of Tunisia. Lampedusa, the main island of the Pelagian Archipelago (Figure 2), consists of an E–W elongated carbonate shelf, about 11 km long and 3 Km wide, with an area of almost 20 km^2 and a maximum topographic elevation of 134 m a.s.l. The island shows a subplanar surface inclined toward the southwest and is carved by deep valleys that connect with the narrow inlets along the coast (Tonielli et al., 2016). The lithological homogeneity (almost totally the late Miocene limestones of the Lampedusa Formation and the Quaternary bioclastic grainstones (Grasso & Pedley, 1985); and the sub-horizontal setting of the strata favoured this tabular morphology deeply incised by several river valleys.

The Lampedusa's shoreline can be divided into two main sectors (Figure 2): the northern coastal domain, mainly exposed to waves driven by Mistral wind, exhibits sub-vertical rocky cliffs with elevations gradually increasing from the east (on average 40–70 m high,) to the west (80 to 130 m high) in agreement with the orographic setting of the island. High coasts also characterize the western and south-western portion of Lampedusa Island with sub-vertical cliffs rising up

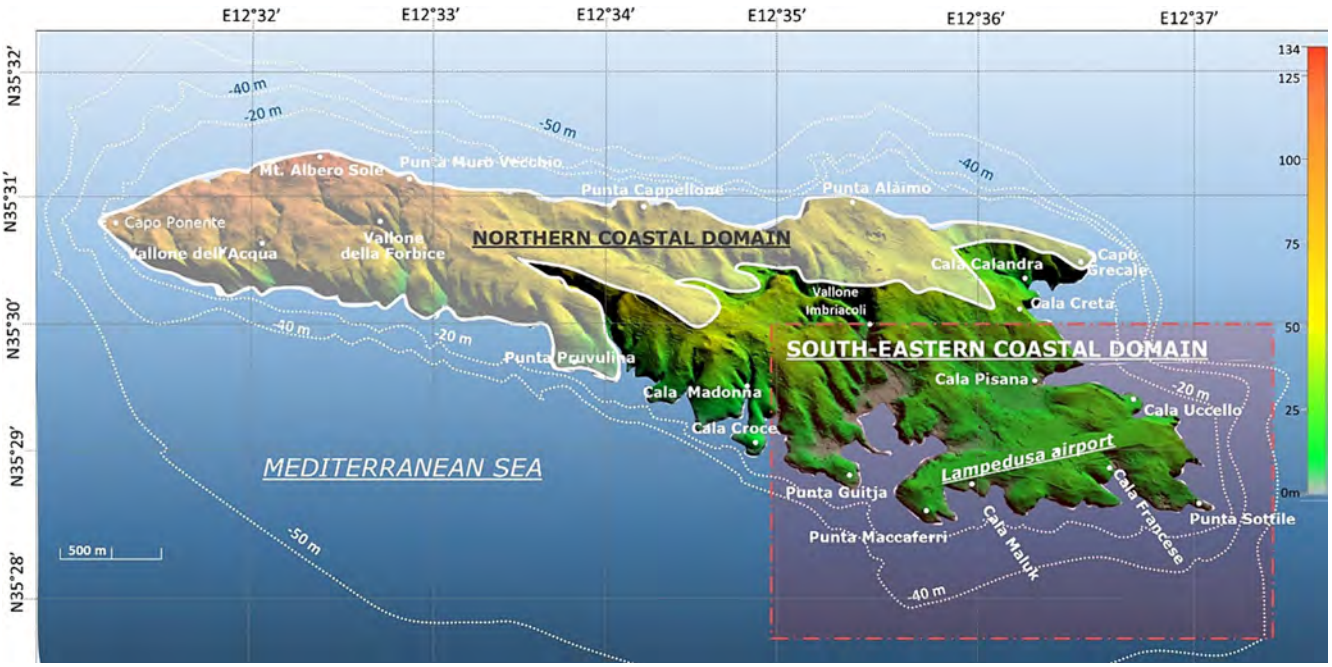

FIGURE 2 Geomorphological setting of Lampedusa Island based on digital terrain model with a spatial resolution 2 × 2 m (https://www.sitr.regione.sicilia.it/geoportale/it/metadata/details/502, last access 24 July 2023). Within the red box, the area study of the south-eastern coastal domain of the island (reference system WGS84 UTM33N – EPSG 32633).

to 100 m a.s.l. Generally, along the northern coastal domain, marine abrasion platforms occur at different elevations suggesting an overall long-term uplift of the island. The south-eastern coastal domain is instead characterized by rather irregular coastal landforms dominated by alternating high- and low-lying coastal morphologies forming a series of bays and headlands with sandy beaches and cliffs inclined by an average of 45° (Distefano et al., 2018, 2019, 2022; Panzera, Sicali, & Lombardo, 2015; Figure 2). Overall, these morphologies describe a rias-type coast, originated by marine ingression in river valleys in response to relative sea level rising or to the subsidence process of the area in response to tilting events.

3 | CALCULATION CHAIN FRAMEWORK AND VALIDATION APPROACH

This section will describe the methodology proposed and applied in this work.

It was necessary to build a calculation chain to link all the modelled processes from the simulation of earthquake events to the propagation of the resulting tsunami wave. The developed calculation chain is characterized, firstly, by modelling the effects of earthquakes on sea level changes offshore using the DELFT-3D software (Roelvink & Banning, 1995; Van Ormondt, Nederhoff, & Van Dongeren, 2020). The elevations of the sea surface (output of DELFT-3D modelling) thus become the inputs for the subsequent propagation. Specifically, the propagation of different sea states associated with various earthquake scenarios, ranging from the −50 m bathymetry to the nearshore zone, has been modelled using the MIKE 21 Flow Model FM (Komen et al., 1996; The Wamdi Group, 1988; Warren & Bach, 1992). Again the output of the latter simulation (surface elevations) becomes input to the next one. Thus, the simulation of tsunami wave propagation onshore over the topography has been conducted using HEC-RAS software.

Figure 3 displays the flowchart summarizing the modelling calculation chain.

The framework was validated through the use of benchmarks on tsunami events documented through the National Oceanic and Atmospheric Administration (NOAA) website.

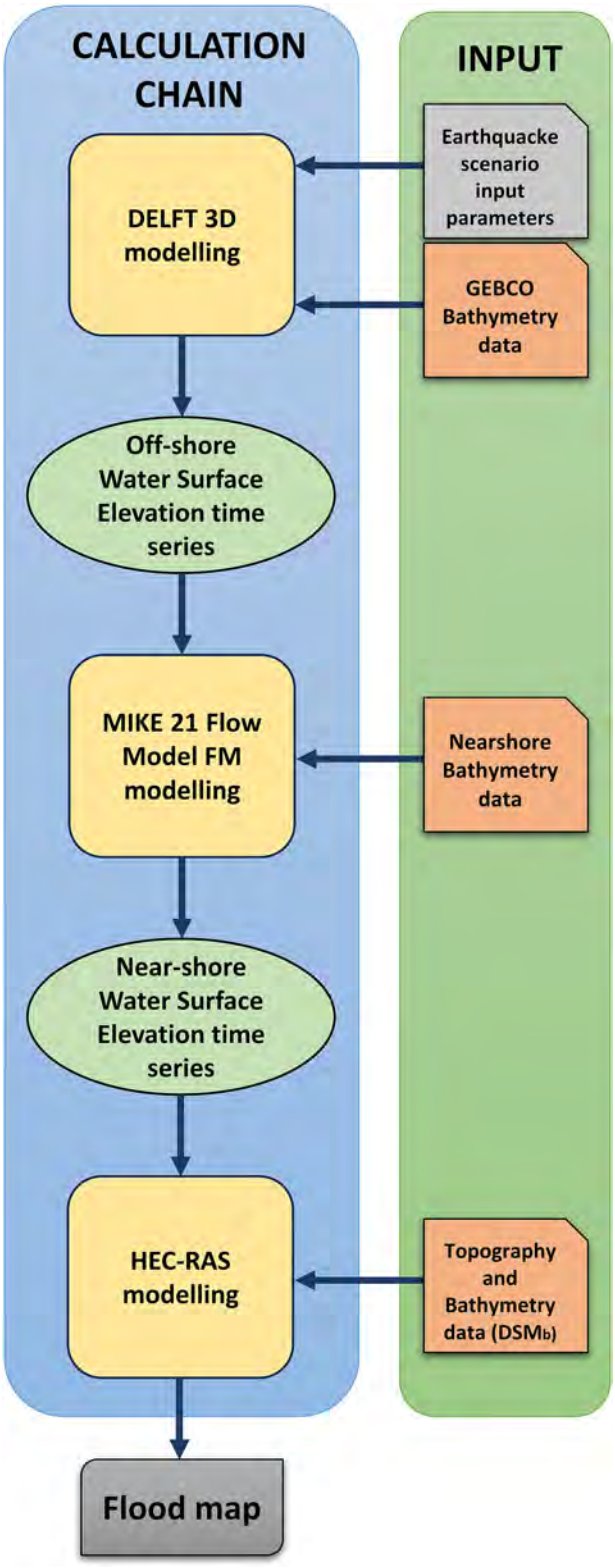

FIGURE 3 Flowchart of the calculation chain used to assess the coastal impact of a tsunami.

3.1 | Validation approach

To assess the adequacy and simulation goodness of the proposed modelling framework we applied the proposed calculation chain and compared the results visually (qualitatively) and numerically (quantitatively) with benchmarks provided by NOOA for the validation process. Specifically, we applied modelling using DELFT-3D to generate two real tsunami events and propagate the tsunami wave from its formation to the offshore area. In particular, the simulated earthquake (and subsequent tsunami) events are Rat Islands (2003), with epicentre location at coordinates 51.13 N, 178.74E and magnitude 7.7 and Unimak (1946), with epicentre location at coordinates 53.32 N 163.19 W and magnitude 8.5 and.

Figure 4 shows the epicentres of the earthquakes used in the validation process (star in red Unimak and in yellow Rat Islands). The respective calculation domains used for propagation with DELFT 3D are indicated in red and dashed yellow. The DART (Deep-ocean Assessment and Reporting of Tsunamis) points (named with IDs 46,401, 46,402 and 46,403) from which the elevation signals for the 2003 Rat Islands tsunami were obtained, are indicated by white dots. The location of the port of Hilo is indicated by the yellow dot. A zoom of the Hilo harbour area with tide gage indication is also shown in the left-bottom corner of Figure 4.

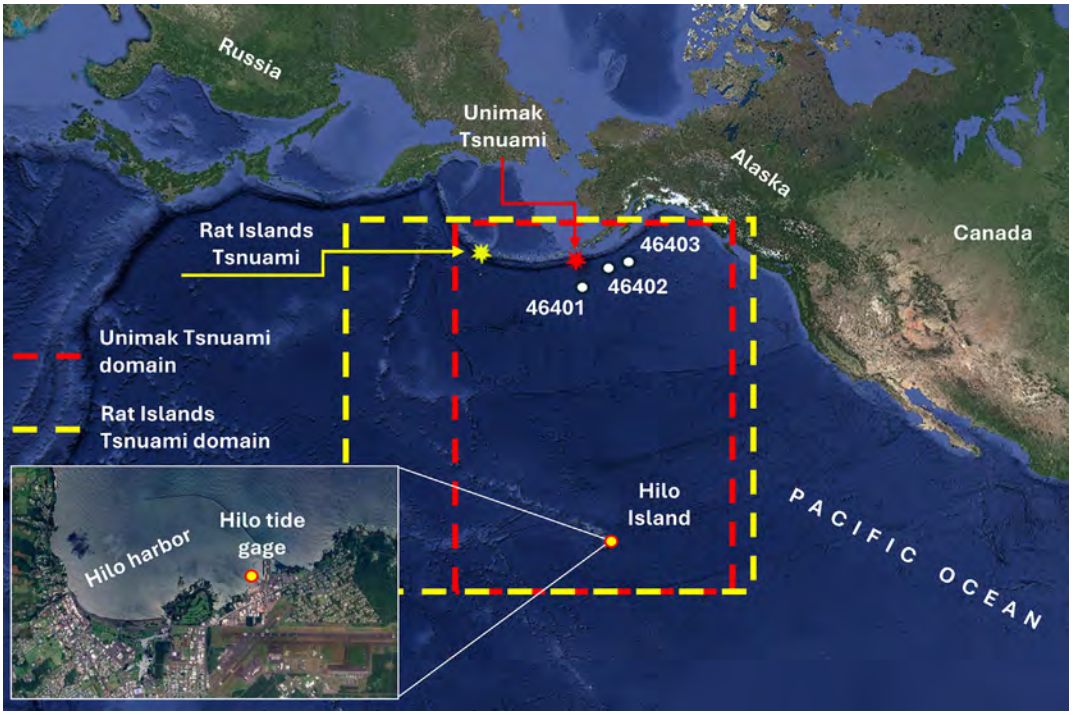

FIGURE 4 The figure illustrates the epicentres of earthquakes utilized in the validation, with the corresponding calculation domains for DELFT 3D propagation marked in red and dashed yellow. White dots indicate DART points (ID: 46401, 46,402 and 46,403) while the yellow dot denotes the port of Hilo. A zoom of Hilo harbour with tide gauge indication is provided in the bottom-left corner of the same figure.

For the first case (Rat Islands), we compared water elevation values at three different locations in the ocean. Specifically, at three DART measuring stations, a system of pressure loggers and buoys was created by NOAA in 2001 for early tsunami detection and the collection of critical data for real-time forecasting. In 2003, from three of these buoys, for the first time in history, tsunami time series forecasting was available for a coastal city prior to the arrival of tsunami waves. For the validation of the first part of the calculation chain (modelling with 3D DELFT), we use three measured DART signals with the signals modelled by the first of the calculation chain models following (Tang, Titov, & Chamberlin, 2009; domain calculation cell size of 450 m and simulation time step of 10 minutes). The agreement between the two signals was computed by calculating the difference between the maximum real and modelled elevation and the minimum (negative) real and modelled elevation. The error was computed through Equation 1 expressed as follows:

$$Error\,[\%] = \frac{Peak_{measured} - Peak_{modeled}}{Peak_{measured}} * 100 \qquad (1)$$

Where $Peak_{measured}$ is the maximum positive elevation value measured and $Peak_{modelled}$ is the maximum positive elevation value obtained from the model.

Similarly, the difference between the recording time of the maximum and minimum peak of real and simulated elevation (time shift/lag between the maxima of the series) was calculated.

For the same event in 2003, we extracted from the DELFT 3D modelling the water level elevation signal at the boundary of the calculation domain used, near Hilo harbour (the most important population centre on the island of Hawaii). This signal was provided as input as a boundary condition to the MIKE 21 model to propagate the wave in the near-shore area and extract the simulated water level elevation values at the Hilo Tide Gages (Figure 6). The computational domain of this second modelling was discretized using an unstructured Delaunay grid and the computational time-step was set to 30 seconds. The measured time series of the surface elevation for the 2003 Rat Islands event at this point is shown in Synolakis et al., 2008 and Tang, Titov, & Chamberlin, 2009. Again, we compared the two signals (measured and modelled) numerically by calculating the correlation coefficient, the RMSE and the difference between the measured maximum and minimum value with the simulated maximum and minimum elevation, respectively. Again, their shifts/lags in time and error were calculated.

On the other hand, the 1946 event was modelled entirely using the calculation chain, having in this case a benchmark on the Hilo harbour inundation presented by Shepard, Macdonald, and Cox (1950). In particular, DELFT 3D was used to generate the tsunami event and the propagation was carried out over the entire computational domain. Using the detailed topo-batimetry (1 × 1 m resolution) from NOOA (https://www.ncei.noaa.gov/maps/bathymetry/) we extracted and used the output signal of DELFT 3D, at the calculation cell closest to Hilo harbour, as the input boundary condition in MIKE 21. In this way, we obtained the sub-coastal water level variations. The extracted elevation values in this area were inserted as input stage hydrographs within the boundary conditions of the computational domain in HEC-RAS to assess the extent of tsunami wave inundation (Figure 7). The result obtained was compared visually and numerically with that reported in Tang, Titov, and Chamberlin (2009). We compared the result of the HEC-RAS modelling with the surveyed inundation values, measured and reported in (Shepard, Macdonald, & Cox, 1950) as well as with the results of the MOST (Method Of Splitting Tsunami) model adopted by NOOA and also reported in (Tang, Titov, & Chamberlin, 2009). Propagation was simulated on the same topo-bathymetric data used by Tang, Titov, and Chamberlin (2009) in order to not affect the results and comparisons. Again, for the

qualitative-comparative assessment the flood extents predicted by the different simulation models (MOST and HEC-RAS) were compared using field observation as ground truth (Shepard, Macdonald, & Cox, 1950). We therefore constructed binary (flood/non-flood) maps with 1 × 1 m resolution for comparison and validation of the methodology. The accuracy of the predicted classification was assessed using different measures of prediction performance, such as accuracy, Matthews correlation coefficient (MCC) and F1 score following Thalakkottukara et al. (2024). The equations (Equations 2, 3, 4, 5 and 6) describing the calculation of the validation metrics are given below.

$$Accuracy = \frac{TP + TN}{TP + TN + FP + FN} \tag{2}$$

$$Precision = \frac{TP}{TP + TF} \tag{3}$$

$$Recall = \frac{TP}{TP + FN} \tag{4}$$

$$F_1 score = 2 * \frac{Precision * Recall}{Precision + Recall} \tag{5}$$

$$MCC = \frac{(TP * TN) - (FP * FN)}{\sqrt{((TP + FP) * (TP + FN) * (TN + FP) * (TN + FN)}} \tag{6}$$

Where TP (true positive) and TN (true negative) denote the count of observed data accurately classified as inundation and non-inundation, respectively. Conversely, false positive (FP) and false negative (FN) indicate the number of data points misclassified.

4 | CASE STUDY: LAMPEDUSA ISLAND

The computational chain was used to assess the effects of tsunami waves, caused by earthquakes in the Hellenic Arc, on the southeast coast of the island of Lampedusa. This section details the materials used and how the calculation chain was used specifically for the case study. Section 4.1 contains a description of all bathymetric and topographic data. Also, the modelling methodologies adopted for the simulation of earthquake magnitude scenarios and the numerical modelling of tsunami wave propagation in offshore, nearshore and onshore areas are presented in sections 4.2, 4.3 and 4.4, respectively.

4.1 | Bathymetric and topographic data

Bathymetric data were collected by the Institute Marine Science of the National Research Council (CNR-ISMAR) of Naples (Italy) around Lampedusa Island from the contribution of the project "Implementation of research activity and monitoring around Pelagie Islands Marine Protected Area", within the project "CAmBiA – Contabilità Ambientale e Bilancio Ambientale" funded by the Ministry of the Environment and Protection of Land and Sea (MATTM – Ministero dell'Ambiente e della Tutela del Territorio e del Mare), directive n° 5,135 of march 2015. The data were acquired down to 50 m of depth, during the oceanographic survey "Lampedusa 2015". The survey was performed using a pole-mounted Reson SeaBat 7,125 400 kHz MBES, providing sub-centimetric resolution. The vessel was equipped with an Omnistar Differential Global Positioning System (DGPS) and an IxSea Octans 3,000 gyrocompass and motion sensor that provided positioning data (with sub-meter accuracy) and attitude data (0.01° accuracy). A Valeport miniSVS sound velocity probe and a sound velocity profiler were used to provide the real-time surficial sound speed for the beam steering and the velocity profile required for the depth computation. The Reson PDS2000 4.1.2.9 version was used for logging and processing MBES bathymetric data: tide data, recorded during acquisition, were applied to all datasets to set up the real depth before starting the despiking process to generate the final contour with a 5 m line spacing (Innangi et al., 2019; Tonielli et al., 2016). The contouring was compiled by integrating the bathymetric data acquired in 2006 in the frame of the former "Mappatura morfo-batimetrica di Lampedusa" project (Coastal Consulting Exploration, 2006; Giardina & De Rubeis, 2012), to complete some areas remaining from the 2015 acquisition. To compensate for the lack of bathymetric data in coastal areas (less than −5 m) and within the port basin, the data acquired from the vessel were integrated with the bathymetric data extrapolated from the *Carta Nautica* of *Marina Militare Italiana* N°. *240 – Isola di Lampedusa*. The complete bathymetric data were then interpolated using linear triangular interpolation to obtain a digital bathymetry with a resolution of 2 × 2 m. Subsequently, the obtained bathymetry was merged, using the raster merge tool in GIS software, with the digital elevation model (DEM) of the *Regione Siciliana* (acquired in 2013), with a resolution of 2 × 2 m, to create a raster encompassing both negative and positive elevation values. Furthermore, to ensure a more accurate propagation of the tsunami wave over the topography, the built-up areas were burned, resulting in an elevation model of the surfaces (DSM). Hereinafter, the comprehensive digital model consisting of bathymetry, topography, and built environment will be referred to as DSM_b. Figure 4 displays the DSM_b, indicating the bathymetric lines and surveyed points used for constructing the detailed bathymetry specifically developed for this study.

4.2 | Offshore tsunami numerical modelling

The offshore tsunami numerical modelling was run through the Delft Dashboard and Delft3D, and the tsunami wave propagation was visualized from the ideal tsunamigenic source within the western Hellenic Arc to the Lampedusa Island with a modelling domain of approximately 600 × 400 km^2. Three scenarios were modelled by using as inputs earthquake rupture parameters (i.e. strike, dip, rake, slip and depth) retrieved from an extensive literature review on Mediterranean Tsunami events to generate earthquakes with estimated Mw 8.5, 7.5 and 6.5 (Table 1). The fault rupture parameters used to simulate offshore tsunami wave generation using Delft3D referred to the most likely scenarios for inducing Mw 8.5, 7.5 and 6.5 earthquakes originating from the western Hellenic Arc. The scenario utilized in this simulation also considered the epicentre, depth and rake of several AD 365 earthquake-tsunami studies conducted by (Ambraseys, 2001; Papadimitriou & Karakostas, 2008; Shaw et al., 2008). An earthquake magnitude of Mw 8.5 can cause tsunami waves comparable to the AD 365 tsunami (Ohsumi, Dohi, & Hazarika, 2018; Papadimitriou & Karakostas, 2008; G. A. Papadopoulos et al., 2014), while Mw 6.5 is

TABLE 1 Earthquake rupture parameters used for the offshore wave propagation. The parameters were extracted from previous studies on past tsunamigenic events detected within the Hellenic Arc that had magnitudes ranging between Mw 6.5 and Mw 8.5 (Ambraseys, 2001; Papadimitriou & Karakostas, 2008; Shaw et al., 2008).

	Rupture scenario's inputs		
Rupture parameter	**1**	**2**	**3**
Strike [°]	113–147	129	133–143
Dip [°]	35	35	35
Length [km]	365	96.7	24.8
Width [km]	80	38.7	15
Rake [°]	90	90	90
Slip [m]	25	25	25
Depth [km]	5	5	5
Magnitude [M_w]	8.5	7.5	6.5

TABLE 2 Selected locations and depths in tsunami propagation simulations using Delft dashboard and Delft3D to determine water levels in the eastern nearshore of Lampedusa, Italy.

DELFT 3D output points	Latitude	Longitude	Depth [m]
1	35.5049	12.6319	49
2	35.4952	12.6370	50
3	35.4853	12.6274	49
4	35.4850	12.4220	50

the lowest magnitude used for a tsunami waves propagation modelling starting in the western Hellenic Arc (Lorito et al., 2008; Ott et al., 2021; Stiros & Papageorgiou, 2001). The bathymetry data used in this part of the modelling chain is GEBCO 19 with a resolution of 15 arc sec or 450 m (Lemenkova, 2020; Novaczek, Devillers, & Edinger, 2019). The Riemann boundary type was adopted to avoid other water level inputs from the boundary due to wave reflection (Van Ormondt, Nederhoff, & Van Dongeren, 2020). The grid type selected is rectangular with a resolution of 500 m. The low resolution was applied because the modelling focuses on the distribution pattern, arrival time and water level of tsunami waves when they reach the nearshore (Laknath et al., 2020; Röbke et al., 2021). Manning roughness coefficient was employed with the advection scheme for momentum in the form of cyclic since numerical modelling only describes offshore tsunami propagation without the involvement of detailed and profound depth of inundation (Engel et al., 2016; Sarker, 2019).

There are four DELFT 3D output points located in the eastern and southeastern parts of Lampedusa, with bathymetry ranging from 49 m to 50 m (Table 2). The simulation of tsunami propagation from the tsunamigenic source offshore to the nearshore implemented linear shallow water equations (equations 1–4) since wave generation has a larger wavelength compared to amplitude (Khan & Kevlahan, 2022). It is estimated that the wavelength is 20 times larger than the water depth (Sugawara, Minoura, & Imamura, 2020). According to the long-wave approach, the vertical acceleration of the fluid is slower than the acceleration of gravity (Liu et al., 2009). Therefore, there is no variation in water pressure at different depths, and the horizontal movement also does not change with depth (Wang & Power, 2011). The linear long-wave equation could describe the movement of tsunamis in the deep sea (Khan & Kevlahan, 2022; Laksono et al., 2020, 2023; Sugawara, Minoura, & Imamura, 2020).

When the tsunamis hit the nearshore zone the wave amplitude is larger than the wavelength. The wave rate decreases but the wave height increases, hence the non-linear shallow water equations are applicable in this propagation phase. In these equations, non-linear convective forces, inertial forces, and bottom friction are more important to consider than Coriolis forces or frequency dispersion (Hu, Mingham, & Causon, 2000; Sánchez-Linares et al., 2015).

4.3 | Nearshore tsunami numerical modelling

For the numerical modelling of the water surface propagation from the bathymetric −50 m to the coast, we used the software MIKE 21 Flow Model FM. This module of MIKE 21 is a widely used and advanced numerical model designed for simulating hydrodynamic processes in coastal and marine environments. The authors used this software to simulate the propagation of water surface elevation from offshore to nearshore.

The MIKE 21 Flow Model FM utilizes the finite volume method to discretize and solve the governing equations of fluid flow. It employs a flexible Delaunay triangular mesh, which allows for efficient representation of irregular coastlines, complex bathymetry and varying spatial resolutions. The flexible triangular mesh adaptively refines the grid in areas of interest, ensuring an accurate representation of nearshore processes and improving computational efficiency. To build the mesh the authors used the Mike Mesh Generator (MMG) by tracing control points within the area of interest. Next, MIKE uses these control points to generate a grid of triangles, where each control point is a vertex of a triangle. Delaunay's triangular grid is constructed to maximize the quality of the triangles, ensuring that each triangle contains only the nearest control points and that there are no points within circumscribed circles of triangles. This grid provides a solid basis for hydraulic analysis and allows for accurate and reliable results. The governing equations used to simulate water surface elevation propagation from offshore to nearshore are the 2D shallow water equations. These equations, derived from the principles of conservation of mass and momentum, describe the behaviour of fluid flow in shallow water conditions. These equations consider the effects of gravity, friction, advection, bottom slope and water surface elevation on the flow behaviour. To simulate the propagation of water surface elevation from offshore to nearshore, appropriate boundary conditions have been specified. The model allows for the application of open boundary conditions, where water surface elevation and velocity were specified at the offshore boundary. For the point values of the free surface elevation (DELFT 3D Output points), Thiessen polygons were calculated on the MIKE 21 calculation domain to identify the dimensions of the boundary conditions (shown in Figure 5). After the simulation, the MIKE 21 Flow Model FM provides a range of output variables, including water surface elevation which is the input data for the model put on HEC-RAS (Brunner, 2016).

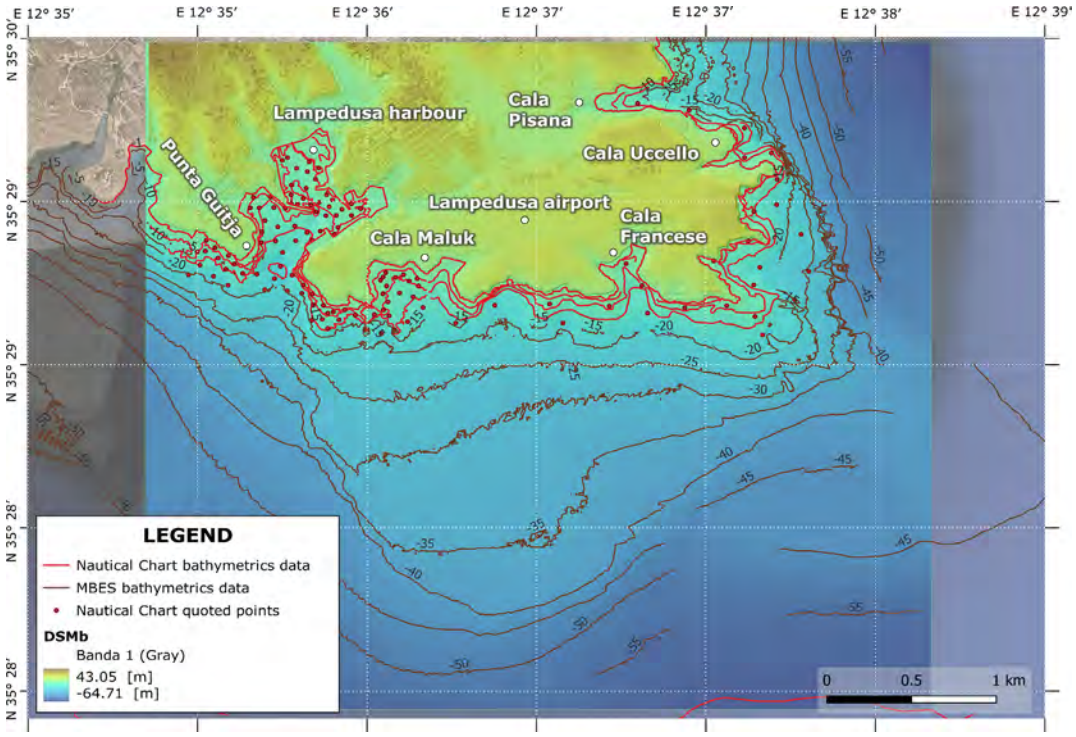

FIGURE 5 DSM_b showing bathymetric lines and surveyed points used in this study (Google satellite imagery in background).

4.4 | Onshore tsunami inundation modelling

In the field of hydraulic engineering and water flow propagation modelling on DEMs, the Hydrologic Engineering Centres-River Analysis System (HEC-RAS) software, developed by the US Army Corps of Engineers Hydrologic Engineering Centre, has gained widespread recognition for its powerful capabilities in river flow, flood and hydraulic analysis simulation.

The authors chose HEC-RAS because it provides a comprehensive platform for water flow simulation, including non-stationary flow conditions, making it suitable for modelling tsunami waves and their propagation (Amaliah & Ginting, 2023; Natarajan & Radhakrishnan, 2020). One of the most important applications of HEC-RAS is the simulation of stage hydrographs, which represent the temporal variation of water levels at a specific location in the computational domain. This simulation is crucial for assessing flood risks, designing flood control measures and understanding flood dynamics. HEC-RAS allows users to input such stage hydrographs and accurately simulate their propagation. To improve the accuracy of flood simulations and hydraulic analysis, HEC-RAS integrates Digital Elevation Models (DEM). By incorporating DEMs, HEC-RAS can take into account the influence of terrain and topography on the flood paths.

The simulation process begins by importing the DSM_b data (that includes topography, building surface and bathymetry data) into HEC-RAS, which defines the underlying terrain. The software then generates a calculation grid (2D flow area) based on the DSM_b, discretizing the floodplain into calculation cells. This grid allows precise calculations of flow velocities, flood depths and extents throughout the study area. A two-dimensional flow area (2D flow area) was created with a spacing of 2 m along both the y-axis and x-axis, which corresponds to the pixel size of the input DSM_b model.

The domain of the model (2D flow area) was digitalized considering both the positive elevation points at the northern boundary of the DSM_b (see Figure 4) and the negative elevation points, extending it to the −1 m bathymetry, which represents the on-shore boundary conditions. To obtain more accurate and precise results, the 'initial stage' function was activated to fill all cells of the calculation grid that are below 0 m with water. In this way, the initial condition is that the event starts in calm sea conditions and with an initial level of 0.

The HEC-RAS software was used to simulate the flood wave flooding the coastal area of Lampedusa, using stage hydrographs as input data. The stage hydrographs, in this case, describe the sea level variation and were therefore used to simulate the tsunami wave contained in the level timeseries.

The stage hydrographs are therefore inserted at the desired positions, in this case at the boundary conditions (Figure 5). From the previous modelling using the MIKE FLOW MODEL FM software (see section 3.3), the water surface elevation time-series at near shore zone were extracted and used as input stage hydrographs in the HEC-RAS model. Thiessen polygons for the MIKE 21 Output Extraction points (hereinafter O. E points) on the HEC-RAS domain were calculated, in order to obtain the boundary condition extensions.

Since the propagation of the wave from the shoreline into the topographic surface can be treated as true mass propagation, due to the large volumes of water involved and the significant kinetic energy. When a tsunami reaches land, it manifests as a series of powerful, fast-moving surges rather than traditional breaking waves. These surges behave like strong and fast-moving tides, capable of travelling far inland and causing extensive damage due to the mass and velocity of the water. This behaviour is supported by studies on tsunami runup and inundation processes (e.g. USGS - https://www.usgs.gov/centers/pcmsc/life-tsunami). The model-solving equations implemented in HEC-RAS allow for an adequate description of the propagation

dynamics of the water surface, which then results in a flood wave in the coastal zone.

The governing equations used in the HEC-RAS model can be classified into two categories: the one-dimensional (1D) Saint-Venant equations and the two-dimensional (2D) shallow water equations. The choice of equations depends on the nature of the flow being simulated. To run the model, shallow water equations (for a 2D simulation) were applied to calculate water surface elevations and flow velocities in each computational cell. Below, we provide an overview of the 2D equations used in this work.

The software then propagates the hydrograph stages downstream, considering the effects of terrain geometry, flow resistance and topographic variations of the DSM_b.

During the simulation, HEC-RAS provides detailed outputs, including water surface profiles, flow velocities and floodplain flood maps.

5 | RESULTS AND DISCUSSIONS

5.1 | Validation results

Figure 6 shows the results of the validation process described in section 3.1.

The first line shows the comparison of the levels measured by the DART stations in blue for the 2003 event and modelled using DELFT 3D in red (subplots A, B and C of Figure 6 for DART measuring stations 46,401, 46,402 and 46,403, respectively). Already from this first comparison, it can be seen that the 3D DELFT modelling succeeded in capturing the real trend of water level elevations following the 2003 Rat Islands earthquake. In particular, the trend of the maximum peak elevation in subplot C and D is well simulated.

The second row shows the validation results on the Hilo Tide Gage for the 2003 event. Subplot D of Figure 6 represents the comparison of the levels measured by the Hilo harbour recording station. In particular, the line in red represents the time series of the level simulated by MIKE 21 while the blue line represents the recorded elevation values). Again, graphically it is possible to appreciate a good correspondence between the measured and modelled levels except for a variation immediately after the peak elevation and small discrepancies in the final hours of the simulation. On the other hand, the subplot E of Figure 6 represents a scatterplot of the points where the measured elevation values are plotted on the x-axis and the modelled values on the y-axis. The line in yellow represents the bisector of the first and third quadrants. The points are homogeneously arranged on the bisector, suggesting graphically a good agreement between the actual and modelled values.

In the last row of Figure 6 (subplot F), the numerical values of the comparison between the max and min value of each measured and modelled time series, the shift/lag time for the same values and the error calculated according to Equation 1 are shown in a table. The maximum wave height detected at station 46,401 (the location most severely affected by the tsunami was 2.09 m, while the observation was 2.18 m (error of 4.3%). The error of the arrival time of the maximum wave (in advance) is less than 1 minute (0.3 minutes). Almost similar results for the maximum and minimum elevation values were also obtained for the other two stations, 46,402 (error of 0.8% and time advance of the maximum peak of 0.8 minutes) and 46,403.

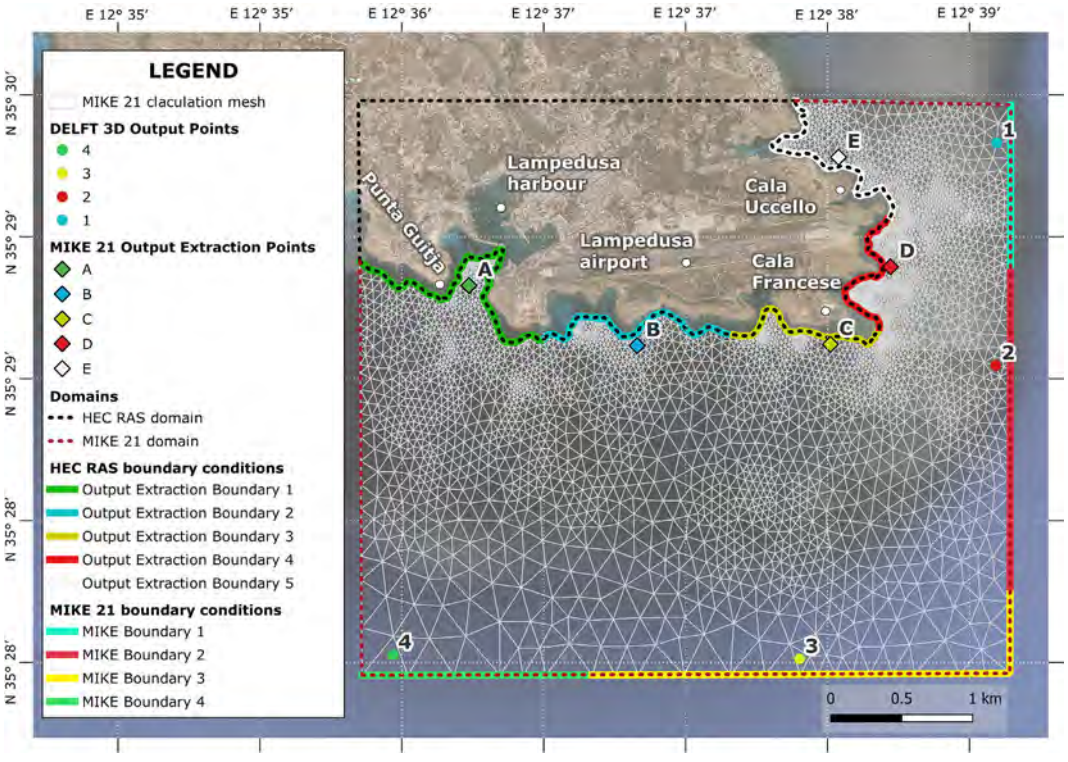

FIGURE 6 Output points of the DELFT 3D modelling and the consequential boundary conditions for the MIKE 21 domain. The output extraction points (A, B, C, D, E) from the free surface in MIKE 21 and the consequential boundary conditions for the HEC-RAS domain are shown in the same figure.

In the latter case, an error of −11% was calculated. As the simulated time series was free of fluctuations (due to the simulation time step used), which were not negligible in relation to the maximum level variations, the variation between the minimum and maximum peaks occurred at different times to the real ones, in fact returning time shifts forward of 5 minutes (peak max) and 10 minutes (peak min).

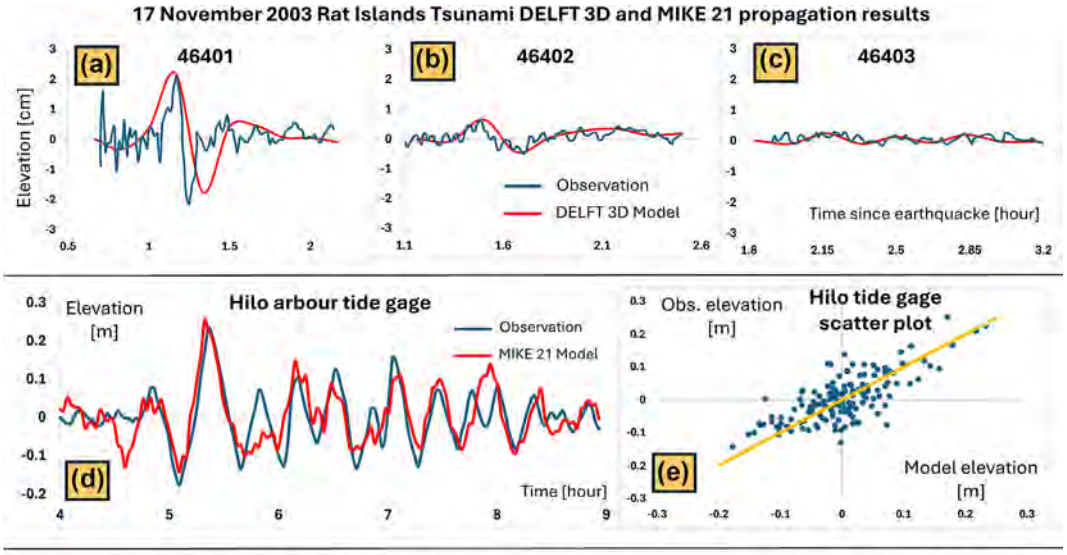

(f)

Modelling point	Max elev. Diff [cm]	Min elev. Diff [cm]	Max peak time lag/shift [min]	Min peak time lag/shift [min]	Correlation coefficient [-]	RMSE	Error [%]
46401	- 0.09	0.4	0.3	-5	-	-	4.3
46402	0.01	0.05	0.8	-2	-	-	0.8
46403	-0.03	0.05	-5	-10	-	-	-11.1
Hilo tide gage	-0.02	0.03	2	1	0.75	0.05	9.2

FIGURE 7 Validation results. The first row showcases comparisons between DART-measured levels (blue) and DELFT 3D-modeled levels (red) for the 2003 event across subplots A, B and C. Subplot D displaying comparisons between measured (blue) and MIKE 21-simulated (red) levels, in Hilo tide gage. Subplot E presents a scatterplot of measured and modelled elevation values. The bottom row (subplot F) presents numerical comparisons and errors between measured and modelled time series.

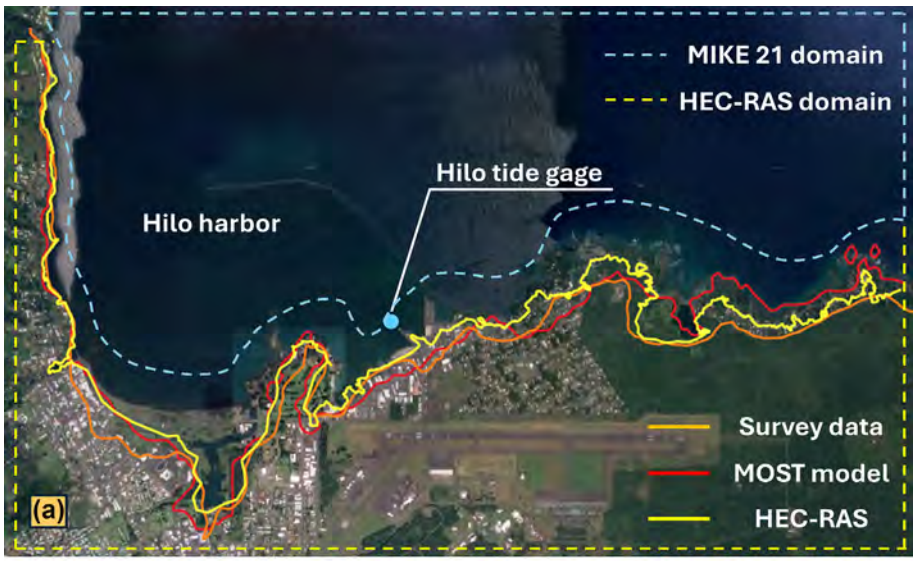

(b)

Model	Accuracy	MCC	Precision	Recall	F1 score
MOST	0.83	0.66	0.78	0.63	0.70
Calculation chain	0.85	0.75	0.94	0.64	0.76

FIGURE 8 Figure 7 presents an overlap analysis of inundation boundaries in the Hilo harbour area, comparing measured max inundation boundaries (Shepard, Macdonald, & Cox, 1950) in red, boundaries modelled via the MOST model (orange), and those obtained through HEC-RAS modelling (yellow). The last row of Figure 7 (subplot B) showcases a comparative analysis of performance metrics between the MOST and HEC-RAS models for mapping inundation areas in the Hilo Island port area.

Similar results were obtained for the simulation with MIKE 21 recorded at the Hilo tide gage. Again, the variations in peak elevation (maximum and minimum) between measured and modelled did not exceed 0.03 cm with a maximum temporal lag of 2 minutes. The overestimation error of the maximum peak elevation is 9%. Finally, the calculated correlation coefficient was 0.75 and the RMSE was 0.05 cm, again suggesting a good agreement between the MIKE 21 modelling and the measured data.

As anticipated in section 3.1 in order to validate the entire calculation chain, including the inundation module, we simulated the

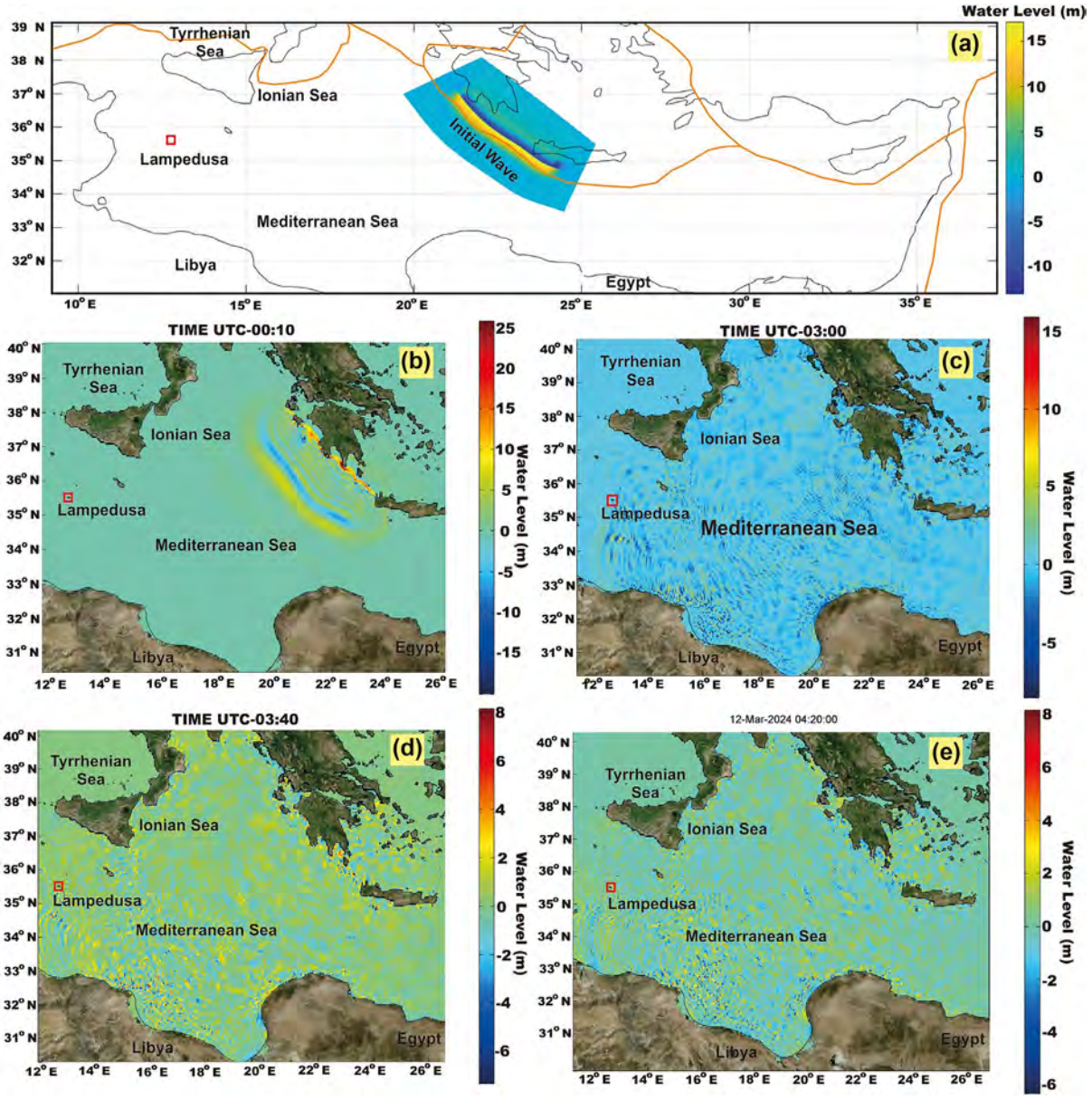

FIGURE 9 a) Initial tsunami wave generation shortly after the Mw 8.5 earthquake and distribution of tsunami waves for the 8.5 Mw scenario at minutes 10 (b), 180 (c), 220 (d) and 260 (e) from the western Hellenic Arc westward toward Lampedusa Island. The maximum run-up height was observed after the 260th minute of tsunami wave generation.

TABLE 3 The maximum run-up height of tsunami waves for the 8.5 Mw scenario measured at Lampedusa is 2.41 m, which is visible in output 2. The average arrival time of the maximum water level at Lampedusa occurred after two hours from the generation of the first tsunami wave offshore.

	I max water level		II max water level	
DELFT 3D output points	Arrival time [minute]	Height [m]	Arrival time [minute]	Height [m]
1	180	1.20	260	2.06
2	165	1.60	260	2.41
3	170	1.58	250	1.74
4	130	0.71	175	1.46

1954 Unimak Tsunami event in its entirety. The results of the inundation simulation for the aforementioned Tsunami are shown in Figure 7.

The first row of Figure 7 (subplot A) shows the overlap over the Hilo harbour area between the measured max inundation boundary (Shepard) (red), the maximum inundation boundary modelled in Tang, Titov, & Chamberlin, 2009 via the MOST model (in orange) and the maximum inundation boundary obtained via the HEC-RAS modelling (in yellow).

It can be seen that in the western part of the area under investigation, the three lines are almost perfectly overlapping. Particularly different is the behaviour further south where the red and yellow lines are similar while completely different (and greater) is the extent of inundation subtended by the orange line. In contrast, in the east, there

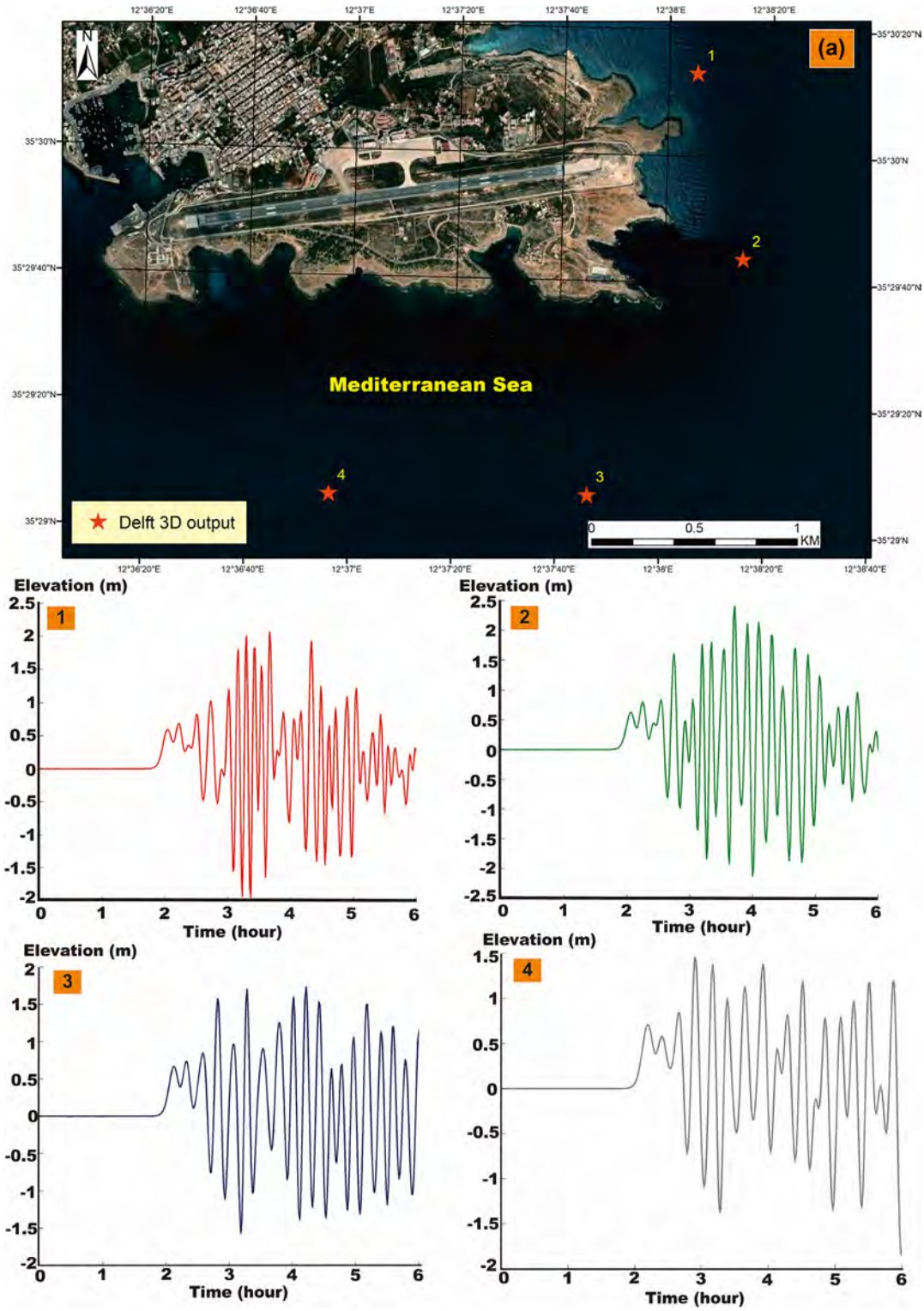

FIGURE 10 Diagram of water level vs tsunami wave arrival time for the 8.5 Mw scenario at output (1), output (2), output (3) and output (4). The maximum run-up heights in outputs 1, 2, 3 and 4 are 2.06 m, 2.41 m, 1.74 m and 1.46 m, respectively. Outputs one to four indicate that the maximum water level prevails in the second phase of the tsunami wave. Each output point location is shown in figure A.

is a better correspondence between orange and yellow while the spread increases for the red line.

To quantify the agreement of the modelling to reality, we analysed the binary flood/non-flood maps described in section 3.5, using the metrics described in the same section. The results of the analysis are shown in the last row of Figure 7.

Subplot B of Figure 7 facilitates the comparison of the various performance metrics of the MOST and HEC-RAS models for mapping the inundation areas of the port area of Hilo Island. The HEC-RAS model classified inundation and non-inundation areas with an accuracy of 85%, which was higher than that of the MOST model (83%). The non-flooded areas were better predicted by the HEC-RAS model than the MOST model, as shown by the high accuracy values (94 vs. 78% respectively). On the other hand, in the prediction of flooded areas, both models perform similarly (HEC-RAS slightly better), as is evident from the recall values (0.63 for MOST and 0.64 for HEC-RAS). The F1 scores also confirm a higher accuracy of HEC-RAS (0.76 vs. 0.7), considering that in this case, the score is independent of the number of data correctly classified as not flooded (Thalakkottukara et al., 2024). Finally, the MCC coefficient yields a high score only when the models predict good results in all four categories of the confusion matrix (i.e. TP, TN, FP and FN), proportional to the size of the inundation and non-inundation datasets, thus again confirming a more than good fit of the HEC-RAS modelling to reality for all categories.

It can thus be seen that all metrics of the HEC-RAS model are more satisfactory than those of the MOST model, thus enabling the validation of the last part of the modelling chain as well.

5.2 | Offshore modelling

Two (7.5 and 6.5 Mw) of the three different scenarios of tsunami offshore wave propagation modelling performed in this study showed quite similar results and rather lower values than the worst-case scenario (8.5 Mw). For this reason, this section describes in detail the calculation of the 8.5 Mw scenario. The tsunami wave propagation from the epicentre of the earthquake at minute 10 to minute 260 is depicted in Figure 8 A, B, C and D, respectively. The tsunami wave impact on the eastern coast of Lampedusa Island would be visible after three hours the seismic activity was started (Figures 6A–C). Therefore, the offshore modelling shows that Lampedusa Island would be hit by the tsunami waves between minutes 180 and 260 (Figure 6C and D). The simulated tsunami waves triggered by the Mw 8.5 earthquake in output 1 display a rise in water level of 0.5 m after 120 minutes of tsunami wave generation in the western Hellenic Arc (Figure 9A). At the 180th minute, the water level reached 1.2 m and then dropped to 0.08 m at the 183rd minute, which is three hours and three minutes after the tsunami waves appeared around the epicentre. At the 190th minute, the water level increased to 1.8 m, and within 30 minutes, the water level reached 2.06 m, which was the maximum wave height at output 1. Thereafter, the water level dropped to 0.71 m within 12 minutes after the maximum water level was attained. In output 2, there was a 0.42 m rise in sea level after 120 minutes from the first generation of tsunami waves (Figure 9B). At the 165th minute, the run-up height reached a maximum of 1.6 m and then decreased to 0.84 m and 0.69 m at the 183rd and 184th minutes, respectively. Eight minutes later, the water level raised to 1.76 m and then started receding in the following minutes. In output 3, the run-up height increased from 0 m at the 105th minute to 0.8 m at the 155th minute (Figure 8C). The maximum run-up height in output 3 was 1.58 m, which occurred 170 minutes after the tsunami wave generation. Subsequently, the water level declined to 0.56 m at the 172nd minute and rebounded until it reached 1.74 m, which was the maximum run-up height of the second phase. The maximum water level was observed at the 250th minute. In output 4, the water level rose from 0 m to 0.66 m between minutes 105 and 130 (Figure 9D). The maximum run-up height of the first phase was 0.71 m, occurring 132 minutes after the offshore tsunami generation.

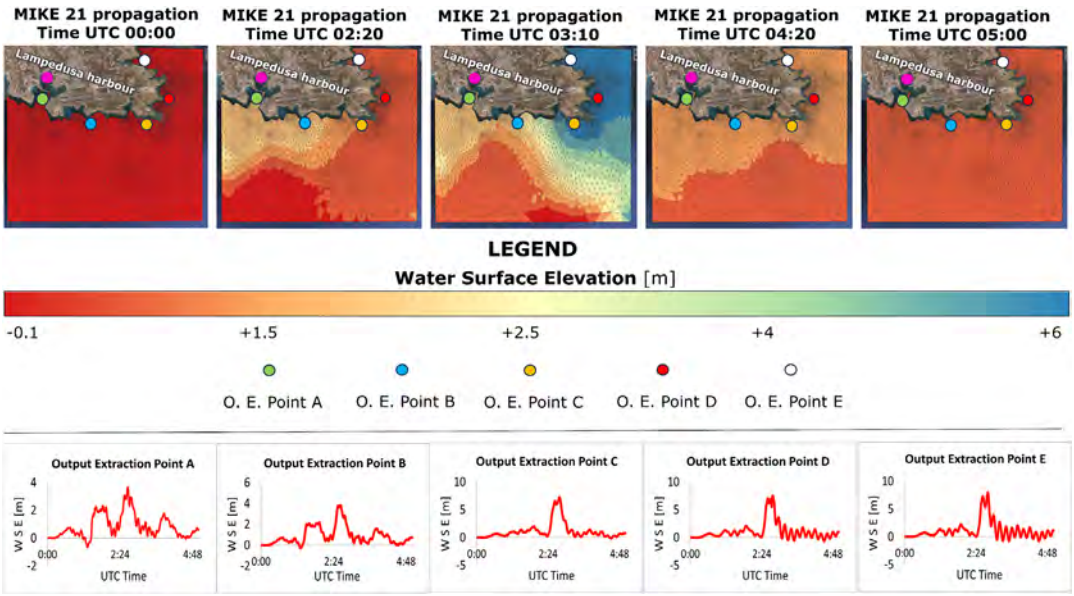

FIGURE 11 Results of the sea state propagation of scenario 8.5. The first line of the figure shows the propagation map at different time instants with an indication of the triangular Delaunay calculation mesh used. In the second line, the mareograms of the MIKE21 O. E. points indicated with different colours in the figure.

The maximum run-up height of the second phase was 1.46 m, reached at the 175th minute. Generally, the water level in the second phase of the run-up is higher than that in the first phase of the run-up. According to Table 3, the maximum run-up height in the second phase ranges between 1.46 m and 2.41 m, while in the first phase, it only ranges between 0.71 m and 1.6 m. Concerning the arrival time of the maximum water level in the first phase of the run-up, it occurred at the 130th–180th minute after the tsunami wave generation, while the second phase of the run-up was identified at the 250th–260th minute.

5.3 | Near shore modelling

The propagation maps of the sea state following offshore to near-shore earthquakes were obtained from the simulation performed on the MIKE 21 FM Flow Model.

Figure 10 displays the results of propagation relative to the Magnitude 8.5 scenario. From the first row of the figure, one can observe the MIKE 21 computational domain, discretized into computational cells according to Delaunay's triangular mesh. The propagation results are represented at various instants of propagation, consistent with

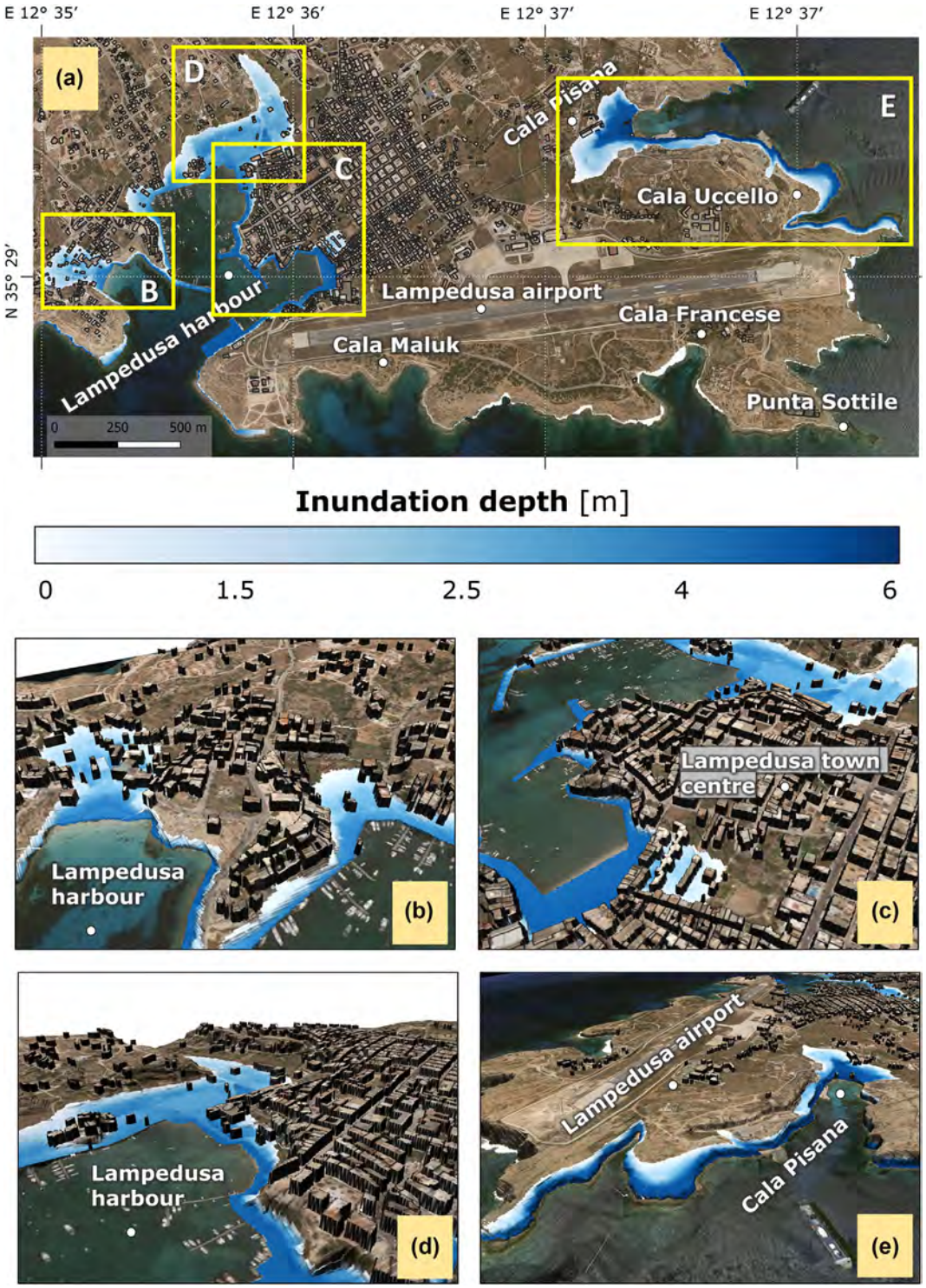

FIGURE 12 Global inundation map for the 8.5 magnitude scenario in subplot A. Subplots B, C, D and E show 3D zooms of the most flooded areas.

those reported in Figure 9. From the onset of propagation, a noticeable rise in sea level due to the tsunami wave propagating towards the coast is evident. Furthermore, the highest values of the free surface are obtained near Cala Pisana and Cala Uccello, the areas directly exposed to the east, the origin and trigger zone of the tsunami. Although, from Figure 9, the elevation values at point 4 are compatible with those at point 1 (for the second maximum run-up height) during propagation, the nearshore elevation values in the port area of Lampedusa do not reach the heights obtained in the east nearshore area of the computational domain. Indeed, phenomena such as greater travel distance of the sea state and refraction cause the tsunami to arrive in the vicinity of Cala Maluk, Punta Sottile, Cala Francese and the port of Lampedusa itself at a lower height.

The second row of Figure 10 represents the mareograms at the O.E. points from the MIKE 21 propagation output map. These points have been placed near the coast and the water elevation values are extracted and used as stage hydrographs for subsequent flood modelling (see section 3.4). O.E. point A is the internal point to the port (green) and is the only point, along with O.E. point B, where there is not a single elevation peak but three. The maximum values reached by the highest peak are 3.5 and 4 m for O.E. points A and B, respectively. As previously discussed, at these points, the wave undergoes more variations during its propagation compared to points C, D and E. For the latter three points, especially for O.E. points D and E, the presence of a single elevated peak is much more pronounced, reaching values close to 7 m in height. After the peak is reached, the mareograms display decreasing periodic oscillations due to rebound phenomena, which accumulate at the end of propagation within the entire computational domain. This behaviour is much more visible for O.E. points D and E since, at these points, the wave arrives earlier than all other points on the cliffs, which act as reflective walls for wave agitation propagation.

The 6.5 and 7.5 magnitude scenario simulations provide very similar results as we found that the relationship between earthquake magnitude and maximum water surface elevation is logarithmic. We have obtained, by simulating also the scenarios of magnitude 6, 7 and 8 (not shown here) that a considerable increase in elevation values (almost always asymptotically towards values near 0 m) was appreciable from magnitude 8 onwards. The knee of the curve is therefore in the vicinity of magnitude 8, which explains why the propagation results of the 6.5 and 7.5 scenarios in this particular case turn out to be very similar.

We decided to not show the propagation graphs and mareograms of scenarios 7.5 and 6.5 which have smaller values, but a brief discussion of these results is provided below. In the 7.5 magnitude scenario (same arguments apply to 6.5 scenario) the peak elevation values (obtained by the mareograms) turn out to be much lower, even near the nearshore area where the maximum values reached by the peaks do not exceed one meter in height for all O.E. points. Even in this scenario, the shape of the mareograms closely resembles that of the 8.5 scenario.

5.4 | Inundation modelling

As mentioned earlier, the results of the MIKE 21 Flow Model FM simulation were used as input for propagation on the topography of the study area. The results of the HEC-RAS modelling for the magnitude 8.5 scenario are shown in Figure 11.

From Figure 11, it can be observed that the areas most affected by flooding in the 8.5 scenario, are those near the small beach inside the harbour. North of this beach, the maximum water depths still reach values of 2.5 m (Sub plot E of Figure 11). This area not only has a low slope but is also located between two higher elevated areas,

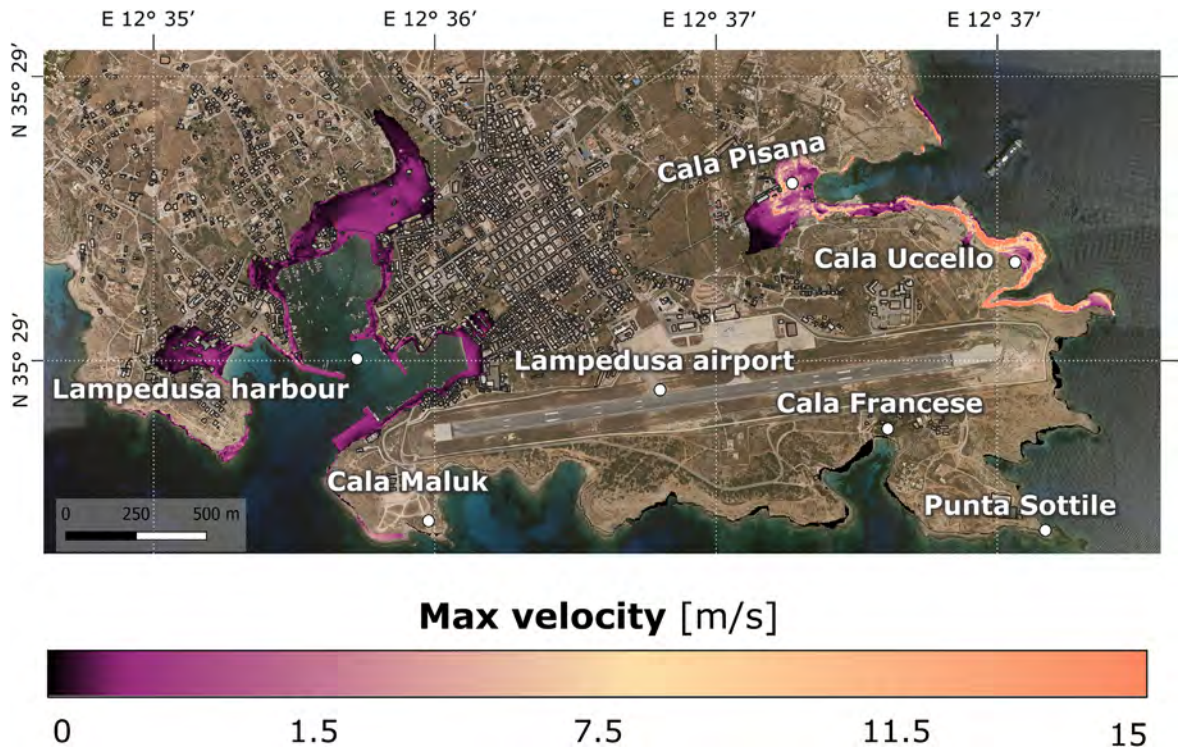

FIGURE 13 Global maximum velocity map for the magnitude 8.5 scenario.

creating a kind of large preferential channel for water discharge. The eastern part of this area is characterized by the urban centre of Lampedusa, which is weakly affected by flooding as it is situated at elevations that are not reached by the higher maximum water depths observed in this area, which are below 4 m (sub plot C of Figure 11). In sub plot B of Figure 11, the most flooded portion of the computational domain, which is also affected by the built environment. This portion of land is located west of the harbour arm, where water depths reach up to 3 m. Even the entire port complex (outer breakwater, vehicular walkway and port platforms), being lower in relation to the rest of the examined topography, is completely flooded in this scenario with maximum water depths of nearly 3.5 m (subplot C of Figure 11).

Finally, even to the east of the computational domain, on the coast of Cala Pisana and Cala Uccello, there is a flooded area despite the coast being predominantly characterized by cliffs. The high wave heights in this area (approximately 8 m) prevent a significant amount of water from being shielded by the coastline (subplot D of Figure 11). Nevertheless, in this case, the flooded area is characterized by a very low percentage of residential buildings. The remaining part of the coast, mainly composed of cliffs, manages to prevent the overtopping of the tsunami wave.

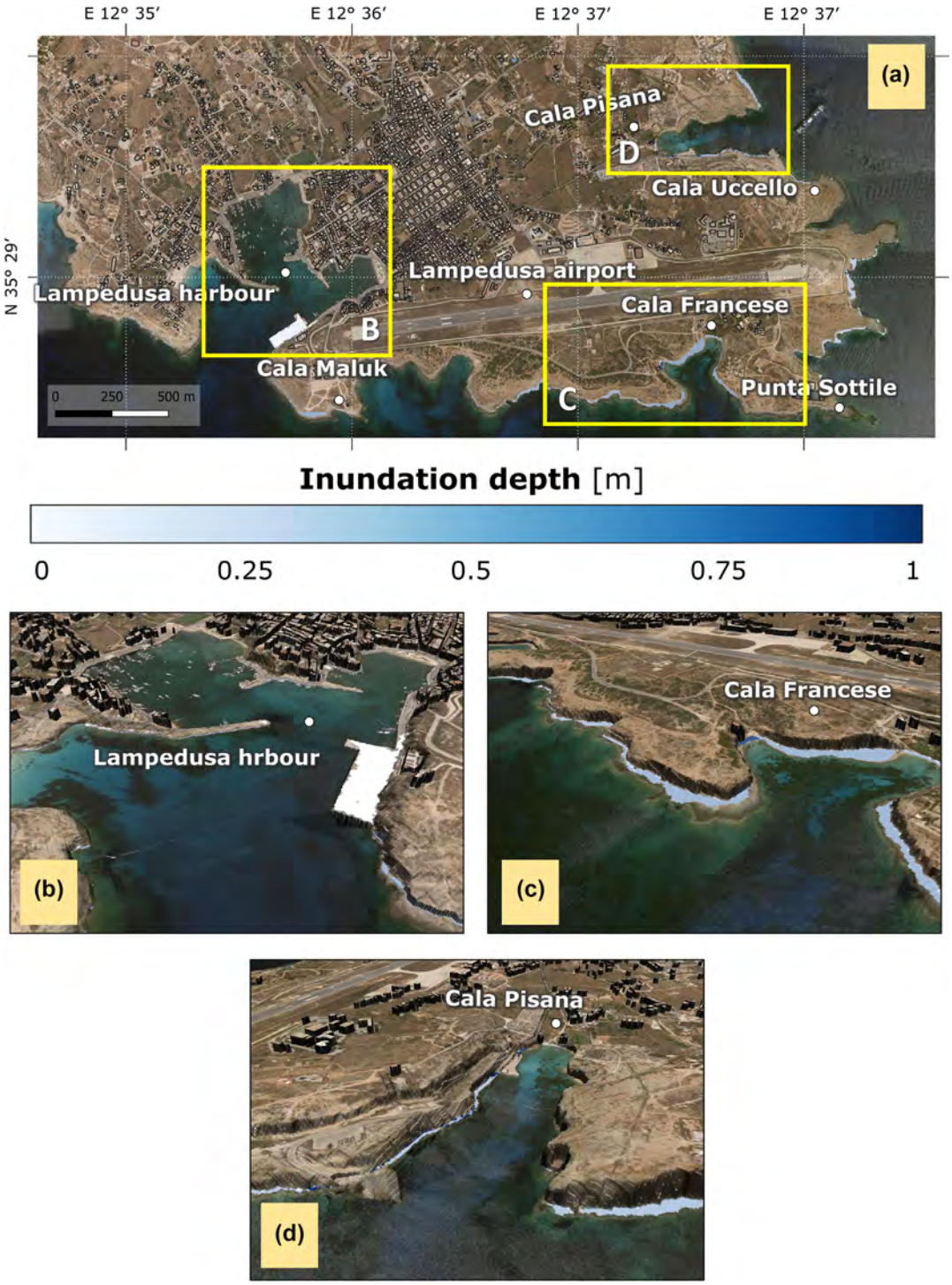

FIGURE 14 Global inundation map for the 7.5 magnitude scenario in subplot A. Subplots B, C and D show 3D zooms of the most flooded areas.

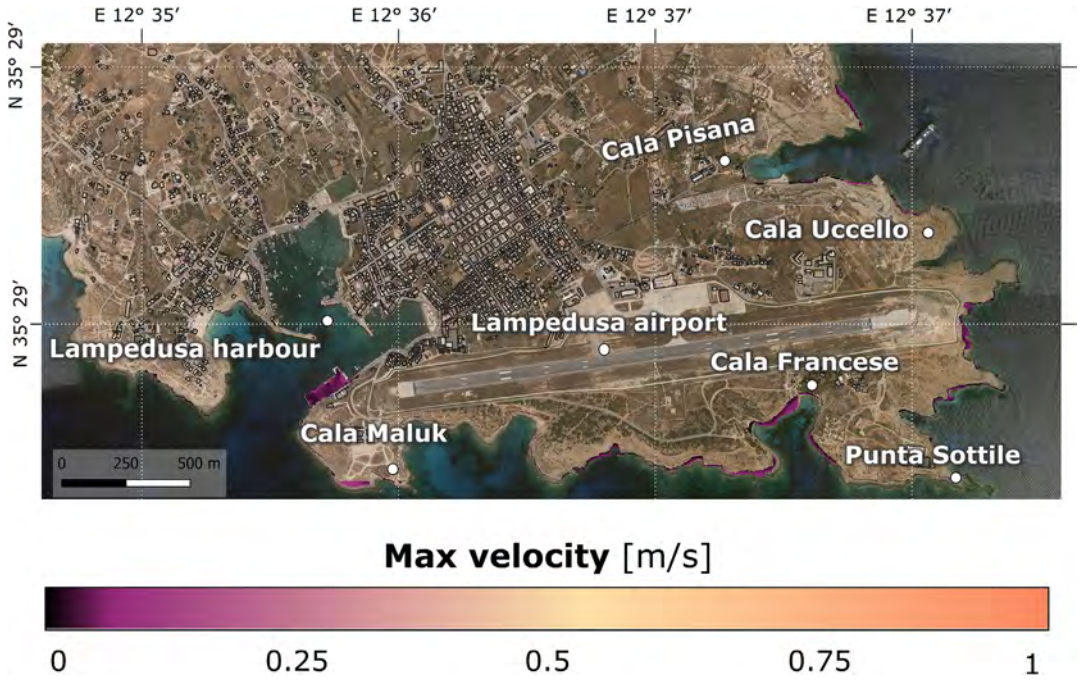

FIGURE 15 Global maximum velocity map for the magnitude 7.5 scenario.

Figure 12 shows the map of the maximum water velocities reached during propagation of the Magnitude 8.5 scenario. Velocity values are low in the harbour area, reaching maximum speeds of about 2 m/s. The highest velocities, with a maximum value of 15 m/s, are reached in the Cala Pisana and Cala Uccello zone, near the cliffs impacted by the tsunami wave. Then velocities rapidly decrease upon the wave's impact with the cliff for the water volumes that continue their propagation. In this area, the steep slope of the topography easily halts the upflow of the discharge.

Figure 13 displays the flooding map related to the magnitude 7.5 scenario. Since the flooded area values for the 6.5 scenario were practically identical to those of the 7.5 scenario (see section 4.3), it was decided to show only the latter map.

From sub plot A of Figure 13, it can be deduced that, in this case, the flooded area is significantly reduced. Even the cliffs to the east (subplot D of Figure 13) manage to contain the waves coming from the same direction, thus preventing any type of flooding. In this case, the maximum water depths, at most 0.5 m, are reached at the cliffs. The wave only causes a rise in sea level at the breaking points on the cliff, while in the harbour area, the outer breakwater and nearby cliffs successfully shield the rise in sea level (sub plot B of Figure 13). The only flooded area within the port structure is identified in the platform south of the harbour arm, but with water depths close to zero. The velocities are also minimal in this case (Figure 14), with overall maximum values below 1 m/s (Figure 15).

6 | CONCLUSIONS

Most of the Mediterranean coastlines are exposed to a high risk of tsunami wave inundation. Coastal areas play a key role in the national economy, they are densely populated and home to commercial, industrial and human-related activities. As such, the impact of a tsunami on the coast could lead to the loss of life and cause serious damage to the local coastal economy. These observations indicate the necessity to thoroughly investigate the propagation of tsunami waves and the extent of tsunami flooding. Indeed, the present study evaluated the risk of flooding due to a tsunami. For this purpose, a three-step model was developed: i) DELFT-3D software was used to simulate the offshore wave propagation from the tsunami source, ii) MIKE 21 Flow Model FM was employed to study nearshore propagation and iii) HEC-RAS was used for onshore tsunami inundation modelling. The calculation chain was validated by applying it to such well-known benchmark sites in the Pacific Ocean and the results were compared to the real cases. The validation process tested that the model has a high level of reliability and the data came out from the three-step model with a well-approximate of the wave propagation simulation with estimated errors lower than 5%. These insights demonstrate that the proposed calculation chain could be a promising tool for the evaluation of tsunami impacts in other contexts, given its scalability and adaptability to different geological contexts and then can be used for accurate tsunami wave simulations not only in the Mediterranean region but also in various case studies. In addition, the research emphasised the importance of taking into account the geomorphology, topography and infrastructure locations of the area under consideration when modelling tsunami propagation and conducting risk assessments. Lampedusa Island in the Mediterranean Sea was selected as a case study due to its high exposure to the risk of tsunamis. However, the island's significant variability in geomorphological features and the critical locations of key infrastructures, such as the port and the airport, which are situated close to the coast, were also contributing factors in its selection for the study. The tsunami wave simulations considered three tsunami scenarios with different magnitudes (Mw 8.5, 7.5, 6.5) generated by hypothetical earthquakes in the Hellenic Arc. The study showcased the potential impacts of high-magnitude earthquakes on the southeastern coast of Lampedusa Island, which hosts most of the main facilities (i.e. port and airport) and local socio-economic activities. The results showed that the Mw

8.5 scenario led to significant flooding in the harbour region, with maximum water depths reaching approximately 3.5 m. The Mw 7.5 scenario demonstrated reduced flooded areas, with the cliffs containing the waves and preventing further flooding. Differences between the Mw 7.5 and Mw 6.5 scenarios were not significant. Indeed, in the worst-case scenario (Mw 8.5), velocity values range between 2 and 15 m/s. The highest velocities are reached at the easternmost part of the Island, at Cala Pisana and Cala Uccello. As demonstrated, the study's methodology can provide valuable insights for estimating tsunami risk and developing emergency management plans. The results of the study also indicated that this approach can be applicable to different geological contexts, providing significant contributions to coastal hazard assessment and mitigation. Moreover, the tsunami propagation computation chain is designed for easy utilization by researchers or technical operators in the field as the numerical computation is not time-consuming and consistently delivers reliable results. As such, the methodology elaborated in this study, with the progressive refinement of this calculation modelling chain in areas with high tsunami hazards, is meant to provide significant contributions to the field of coastal hazard assessment and mitigation.

AUTHOR CONTRIBUTIONS

Conceptualization: Laura Borzì, Agata Di Stefano, Salvatore Distefano. *Methodology* (including methodology development): Laura Borzì, Salvatore Distefano, Sara Innangi, Giorgio Manno, Pietro Scala, FX Anjar Tri Laksono; *Investigation* (data collection): Salvatore Distefano, Sara Innangi. *Software elaboration*: Laura Borzì, Giorgio Manno, Pietro Scala, FX Anjar Tri Laksono. *Writing-initial draft*, *reviewing and editing*: Laura Borzì, Salvatore Distefano, Sara Innangi, Giorgio Manno, Pietro Scala, FX Anjar Tri Laksono. *Final reviewing and supervision*: Giuseppe Ciraolo, Agata Di Stefano, Gamberi Fabiano, Jànos Kovàcs. *Funding acquisition*: Agata Di Stefano (Simit-Tharsy Project - Interreg V-A Italia-Malta - PP3). Giuseppe Ciraolo (Simit-Tharsy Project - Interreg V-A Italia-Malta - PP2).

ACKNOWLEDGEMENTS

Giorgio Manno is supported by the RETURN Extended Partnership funded by the European Union – Next Generation-EU (National Recovery and Resilience Plan – NRRP, Mission 4, Component 2, Investment 1.3 – D.D. 1243 2/8/2022, PE0000005). Open access publishing facilitated by Universita degli Studi di Palermo, as part of the Wiley - CRUI-CARE agreement.

ORCID

Laura Borzì https://orcid.org/0000-0003-3356-7946
Pietro Scala https://orcid.org/0000-0002-6230-0506
F. X. Anjar Tri Laksono https://orcid.org/0000-0002-6061-6136

REFERENCES

Altinok, Y., Alpar, B., Özer, N. & Aykurt, H. (2011) Revision of the tsunami catalogue affecting Turkish coasts and surrounding regions. *Natural Hazards and Earth System Sciences*, 11(2), 273–291. Available from: https://doi.org/10.5194/nhess-11-273-2011

Álvarez-Gómez, J.A., Aniel-Quiroga, Í., González, M. & Otero, L. (2011) Tsunami hazard at the Western Mediterranean Spanish coast from seismic sources. *Natural Hazards and Earth System Sciences*, 11(1), 227–240. Available from: https://doi.org/10.5194/nhess-11-227-2011

Álvarez-Gómez, J.A., Herrero-Barbero, P. & Martínez-Díaz, J.J. (2023) Seismogenic potential and tsunami threat of the strike-slip Carboneras fault in the western Mediterranean from physics-based earthquake simulations. *Natural Hazards and Earth System Sciences*, 23(6), 2031–2052. Available from: https://doi.org/10.5194/nhess-23-2031-2023

Amaliah, R. & Ginting, B.M. (2023) Investigating the capability of HEC-RAS model for tsunami simulation. *Journal of the Civil Engineering Forum*, 9, 161–180. Available from: https://doi.org/10.22146/jcef.6140

Ambraseys, N.N. (2001) Far-field effects of eastern Mediterranean earthquakes in Lower Egypt. *Journal of Seismology*, 5(2), 263–268. Available from: https://doi.org/10.1023/A:1011476718680

Brunner, G.W. (2016) *HEC-RAS River analysis system User's manual version 5.0*. 609 Second Street Davis, CA 95616–4687: US Army Corps of Engineers Institute for Water Resources Hydrologic Engineering Center (HEC).

Coastal Consulting Exploration. (2006) Rilievi marini finalizzati allo studio della morfologia e batimetria dei fondali dell'isola di Lampedusa (p. 26) [Internal Technical Report of Marine Protected Area, Lampedusa, Italy].

Distefano, S., Baldassini, N., Barbagallo, V., Borzì, L., D'Andrea, N.M., Urso, S., et al. (2022) 3D flooding maps as response to tsunami events: applications in the central Sicilian Channel (southern Italy). *Journal of Marine Science and Engineering*, 10(12), 1953. Available from: https://doi.org/10.3390/jmse10121953

Distefano, S., Gamberi, F., Baldassini, N. & Di Stefano, A. (2019) Neogene stratigraphic evolution of a tectonically controlled continental shelf: the example of the Lampedusa island. *Italian Journal of Geosciences*, 138(3), 418–431. Available from: https://doi.org/10.3301/IJG.2019.17

Distefano, S., Gamberi, F., Baldassini, N. & Di Stefano, A. (2021a) Quaternary evolution of coastal plain in response to sea-level changes: example from south-East Sicily (southern Italy). *Water*, 13(11), 1524. Available from: https://doi.org/10.3390/w13111524

Distefano, S., Gamberi, F., Baldassini, N. & Stefano, A.D. (2018) Late Miocene to quaternary structural evolution of the Lampedusa Island offshore. *Geografia Fisica e Dinamica Quaternaria*, 41, 17–31. Available from: https://doi.org/10.4461/GFDQ.2018.41.10

Distefano, S., Gamberi, F., Borzì, L. & Di Stefano, A. (2021b) Quaternary coastal landscape evolution and sea-level rise: an example from south-East Sicily. *Geosciences*, 11(12), 506. Available from: https://doi.org/10.3390/geosciences11120506

Engel, M., Oetjen, J., May, S.M. & Brückner, H. (2016) Tsunami deposits of the Caribbean – towards an improved coastal hazard assessment. *Earth-Science Reviews*, 163, 260–296. Available from: https://doi.org/10.1016/j.earscirev.2016.10.010

England, P., Howell, A., Jackson, J. & Synolakis, C. (2015) Palaeotsunamis and tsunami hazards in the eastern Mediterranean. *Philosophical Transactions of the Royal Society a: Mathematical, Physical and Engineering Sciences*, 373(2053), 20140374. Available from: https://doi.org/10.1098/rsta.2014.0374

Faccenna, C., Funiciello, F., Giardini, D. & Lucente, P. (2001) Episodic back-arc extension during restricted mantle convection in the Central Mediterranean. *Earth and Planetary Science Letters*, 187(1-2), 105–116. Available from: https://doi.org/10.1016/S0012-821X(01)00280-1

Finetti, I., Lentini, F., Carbone, S., Ben, A.D., Stefano, A., Forlin, E., et al. (2005) *Geological outline of Sicily and lithospheric Tectono-dynamics of its Tyrrhenian margin from new CROP seismic data*. Trieste, Italy: Elsevier. Available from: https://www.semanticscholar.org/paper/Geological-Outline-of-Sicily-and-Lithospheric-of-Finetti-Lentini/0a8e202cc45098d8b39b82a95bb7512417fddca6

Giardina, F. & De Rubeis, P. (2012) Analisi della prateria a Posidonia oceanica (L.) Delile (Najadales, Potamogetonaceae) dell' isola di Lampedusa (AMP "Isole Pelagie", Canale di Sicilia). *Bollettino Accademia Gioenia Science Nature*, 45(375), 651–664.

Goes, S., Giardini, D., Jenny, S., Hollenstein, C., Kahle, H.-G. & Geiger, A. (2004) A recent tectonic reorganization in the south-Central Mediterranean. *Earth and Planetary Science Letters*, 226(3–4), 335–345. Available from: https://doi.org/10.1016/j.epsl.2004.07.038

Grasso, M. & Pedley, M.H. (1985) The Pelagian Islands: a new geological interpretation from sedimentological and tectonic studies and its bearing on the evolution of the Central Mediterranean Sea (Pelagian block). *Geologica Romana*, 24, 13–34.

Gutscher, M.-A., Roger, J., Baptista, M.-A., Miranda, J.M. & Tinti, S. (2006) Source of the 1693 Catania earthquake and tsunami (southern Italy): new evidence from tsunami modeling of a locked subduction fault plane. *Geophysical Research Letters*, 33(8), L08309. Available from: https://doi.org/10.1029/2005GL025442

Heidarzadeh, M. & Gusman, A.R. (2021) Source modeling and spectral analysis of the Crete tsunami of 2nd May 2020 along the Hellenic subduction zone, offshore Greece. *Earth, Planets and Space*, 73(1), 74. Available from: https://doi.org/10.1186/s40623-021-01394-4

Heidarzadeh, M., Gusman, A.R. & Mulia, I.E. (2023) The landslide source of the eastern Mediterranean tsunami on 6 February 2023 following the mw 7.8 Kahramanmaraş (Türkiye) inland earthquake. *Geoscience Letters*, 10(1), 50. Available from: https://doi.org/10.1186/s40562-023-00304-8

Heinrich, P., Dupont, A., Menager, M., Trilla, A., Gailler, A., Delouis, B., et al. (2024) Simulation of the Mediterranean tsunami generated by the mw 6.0 event offshore Bejaia (Algeria) on 18 march 2021. *Geophysical Journal International*, 237(3), 1400–1413. Available from: https://doi.org/10.1093/gji/ggae121

Hu, K., Mingham, C.G. & Causon, D.M. (2000) Numerical simulation of wave overtopping of coastal structures using the non-linear shallow water equations. *Coastal Engineering*, 41(4), 433–465. Available from: https://doi.org/10.1016/S0378-3839(00)00040-5

Innangi, S., Tonielli, R., Romagnoli, C., Budillon, F., Di Martino, G., Innangi, M., et al. (2019) Seabed mapping in the Pelagie Islands marine protected area (Sicily Channel, southern Mediterranean) using remote sensing object based image analysis (RSOBIA). *Marine Geophysical Research*, 40(3), 333–355. Available from: https://doi.org/10.1007/s11001-018-9371-6

Khan, R.A. & Kevlahan, N.K.R. (2022) Data assimilation for the two-dimensional shallow water equations: optimal initial conditions for tsunami modelling. *Ocean Modelling*, 174, 102009. Available from: https://doi.org/10.1016/j.ocemod.2022.102009

Komen, G.J., Cavaleri, L., Donelan, M., Hasselmann, K., Hasselmann, S. & Janssen, P.A.E.M. (1996) Dynamics and Modelling of Ocean Waves. In Dynamics and Modelling of Ocean Waves. Available from: https://ui.adsabs.harvard.edu/abs/1996dmow.book.....K

Kron, W. (2013) Coasts: the high-risk areas of the world. *Natural Hazards*, 66(3), 1363–1382. Available from: https://doi.org/10.1007/s11069-012-0215-4

Laknath, D.P.C., Josiah, N.R., Sewwandi, K.A.H.S. & Araki, S. (2020) Simulation of 2004 tsunami inundation in Galle City in Sri Lanka and revisit the present evacuation measures. *Coastal Engineering Proceedings*, 36v, 36. Available from: https://doi.org/10.9753/icce.v36v.papers.36

Laksono, F.A.T., Aditama, M.R., Setijadi, R. & Ramadhan, G. (2020) Run-up height and flow depth simulation of the 2006 South Java tsunami using COMCOT on Widarapayung Beach. *IOP Conference Series: Materials Science and Engineering.*, 982(1), 012047. Available from: https://doi.org/10.1088/1757-899X/982/1/012047

Laksono, F.A.T., Borzi, L., Distefano, S., Czirok, L., Halmai, Á., Di Stefano, A., et al. (2023) Shoreline change dynamics along the Augusta coast, eastern Sicily, South Italy. *Earth Surface Processes and Landforms*, 48(13), 2630–2641. Available from: https://doi.org/10.1002/esp.5644

Laksono, F.A.T., Borzì, L., Distefano, S., Di Stefano, A. & Kovács, J. (2022) Shoreline prediction modelling as a base tool for coastal management: the Catania plain case study (Italy). *Journal of Marine Science and Engineering*, 10(12), 1988. Available from: https://doi.org/10.3390/jmse10121988

Lemenkova, P. (2020) Java and Sumatra segments of the sunda trench: geomorphology and geophysical settings analysed and visualized by GMT. *Bulletin of the Serbian Geographical Society*, 100(2), 1–23. Available from: https://doi.org/10.2298/GSGD2002001L

Liu, Y., Shi, Y., Yuen, D.A., Sevre, E.O.D., Yuan, X. & Xing, H.L. (2009) Comparison of linear and nonlinear shallow wave water equations applied to tsunami waves over the China Sea. *Acta Geotechnica*, 4(2), 129–137. Available from: https://doi.org/10.1007/s11440-008-0073-0

Lo Re, C., Manno, G., Basile, M., Ferrotto, M.F., Cavaleri, L. & Ciraolo, G. (2022) Tsunami vulnerability evaluation for a small Ancient Village on eastern Sicily coast. *Journal of Marine Science and Engineering*, 10(2), 268. Available from: https://doi.org/10.3390/jmse10020268

Lo Re, C., Manno, G. & Ciraolo, G. (2020) Tsunami propagation and flooding in Sicilian coastal areas by means of a weakly dispersive Boussinesq model. *Water*, 12(5), 1448. Available from: https://doi.org/10.3390/w12051448

Lorito, S., Tiberti, M.M., Basili, R., Piatanesi, A. & Valensise, G. (2008) Earthquake-generated tsunamis in the Mediterranean Sea: scenarios of potential threats to southern Italy. *Journal of Geophysical Research: Solid Earth*, 113(B1), 301. Available from: https://doi.org/10.1029/2007JB004943

Maramai, A., Brizuela, B. & Graziani, L. (2014) The Euro-Mediterranean tsunami catalogue. *Annals of Geophysics*, 57(4), 4. Available from: https://doi.org/10.4401/ag-6437

Masina, M., Archetti, R., Besio, G. & Lamberti, A. (2017) Tsunami taxonomy and detection from recent Mediterranean tide gauge data. *Coastal Engineering*, 127, 145–169. Available from: https://doi.org/10.1016/j.coastaleng.2017.06.007

Menager, M., Guilhem Trilla, A. & Delouis, B. (2023) An automated earthquake detection and characterization tool for rapid earthquake and tsunami response in Western Mediterranean. *Geophysical Journal International*, 234(2), 998–1011. Available from: https://doi.org/10.1093/gji/ggad115

Mueller, C., Micallef, A., Spatola, D. & Wang, X. (2020) The tsunami inundation Hazard of the Maltese islands (Central Mediterranean Sea): a submarine landslide and earthquake tsunami scenario study. *Pure and Applied Geophysics*, 177(3), 1617–1638. Available from: https://doi.org/10.1007/s00024-019-02388-w

Natarajan, S. & Radhakrishnan, N. (2020) An integrated hydrologic and hydraulic flood modeling study for a medium-sized ungauged urban catchment area: a case study of Tiruchirappalli City using HEC-HMS and HEC-RAS. *Journal of the Institution of Engineers (India): Series a*, 101(2), 381–398. Available from: https://doi.org/10.1007/s40030-019-00427-2

Novaczek, E., Devillers, R. & Edinger, E. (2019) Generating higher resolution regional seafloor maps from crowd-sourced bathymetry. *PLoS ONE*, 14(6), e0216792. Available from: https://doi.org/10.1371/journal.pone.0216792

Ohsumi, T., Dohi, Y. & Hazarika, H. (2018) Strong motion and tsunami related to the AD 365 Crete earthquake. *Journal of Disaster Research*, 13(5), 943–956. Available from: https://doi.org/10.20965/jdr.2018.p0943

Ott, R.F., Wegmann, K.W., Gallen, S.F., Pazzaglia, F.J., Brandon, M.T., Ueda, K., et al. (2021) Reassessing eastern Mediterranean tectonics and earthquake Hazard from the 365 CE earthquake. *AGU Advances*, 2(2). Available from: https://doi.org/10.1029/2020av000315

Panzera, F., Sicali, S. & Lombardo, G. (2015, July 20) Seismic site response at Lampedusa island, Italy.

Papadimitriou, E.E. & Karakostas, V.G. (2008) Rupture model of the great AD 365 Crete earthquake in the southwestern part of the Hellenic Arc. *Acta Geophysica*, 56(2), 293–312. Available from: https://doi.org/10.2478/s11600-008-0001-6

Papadopoulos, G., Daskalaki, E., Fokaefs, A. & Giraleas, N. (2007) Tsunami hazard in the eastern Mediterranean Sea: strong earthquakes and tsunamis in the West Hellenic Arc and trench system. *Journal of Earthquake and Tsunami*, 4(1), 57–64. Available from: https://doi.org/10.5194/nhess-7-57-2007

Papadopoulos, G. & Fokaefs, A. (2005) Strong tsunamis in the mediterranean sea: a re-evaluation. *ISET Journal of Earthquake Technology*, 42(4), 159–170.

Papadopoulos, G. & Papageorgiou, A. (2014) Large earthquakes and tsunamis in the Mediterranean and its connected seas (pp. 252–266).

Papadopoulos, G.A., Gràcia, E., Urgeles, R., Sallares, V., De Martini, P.M., Pantosti, D., et al. (2014) Historical and pre-historical tsunamis in the Mediterranean and its connected seas: geological signatures, generation mechanisms and coastal impacts. *Marine Geology*, 354,

81–109. Available from: https://doi.org/10.1016/j.margeo.2014.04.014

Papazachos, B. (1996) Large seismic faults in the Hellenic arc. *Annals of Geophysics*, 39(5), Available from: https://doi.org/10.4401/ag-4023

Pararas-Carayannis, G. (2011) The earthquake and tsunami of July 21, 365 AD in the eastern Mediterranean Sea—review of impact on the ancient world—assessment of recurrence and future impact. *Science of Tsunami Hazards*, 30(4), 253–292.

Peresan, A. & Hassan, H.M. (2024) Scenario-based tsunami hazard assessment for northeastern Adriatic coasts. *Mediterranean Geoscience Reviews*, 6(2), 87–110. Available from: https://doi.org/10.1007/s42990-024-00114-w

Polonia, A., Vaiani, S.C. & De Lange, G.J. (2016) Did the a.D. 365 Crete earthquake/tsunami trigger synchronous giant turbidity currents in the Mediterranean Sea? *Geology*, 44(3), 191–194. Available from: https://doi.org/10.1130/G37486.1

Röbke, B.R., Leijnse, T., Winter, G., van Ormondt, M., van Nieuwkoop, J. & de Graaff, R. (2021) Rapid assessment of tsunami offshore propagation and inundation with d-flow flexible mesh and sfincs for the 2011 tōhoku tsunami in Japan. *Journal of Marine Science and Engineering*, 9(5), 453. Available from: https://doi.org/10.3390/jmse9050453

Roelvink, J.A. & Banning, G.K.F.M.V. (1995) Design and development of DELFT3D and application to coastal morphodynamics. *Oceanographic Literature Review*, 11(42), 925.

Royden, L.H. & Papanikolaou, D.J. (2011) Slab segmentation and late Cenozoic disruption of the Hellenic arc. *Geochemistry, Geophysics, Geosystems*, 12(3), Available from: https://doi.org/10.1029/2010GC003280

Salamon, A., Rockwell, T., Guidoboni, E. & Comastri, A. (2011) A critical evaluation of tsunami records reported for the Levant coast from the second millennium BCE to the present. *Israel Journal of Earth Sciences*, 58(3), 327–354. Available from: https://doi.org/10.1560/IJES.58.2-3.327

Sánchez-Linares, C., de la Asunción, M., Castro, M.J., Mishra, S. & Šukys, J. (2015) Multi-level Monte Carlo finite volume method for shallow water equations with uncertain parameters applied to landslides-generated tsunamis. *Applied Mathematical Modelling*, 39(23), 7211–7226. Available from: https://doi.org/10.1016/j.apm.2015.03.011

Sarker, M.A. (2019) Numerical modelling of tsunami in the Makran subduction zone–a case study on the 1945 event. *Journal of Operational Oceanography*, 12(sup2), S212–S229. Available from: https://doi.org/10.1080/1755876X.2018.1527883

Shaw, B., Ambraseys, N.N., England, P.C., Floyd, M.A., Gorman, G.J., Higham, T.F.G., et al. (2008) Eastern Mediterranean tectonics and tsunami hazard inferred from the AD 365 earthquake. *Nature Geoscience*, 1(4), 268–276. Available from: https://doi.org/10.1038/ngeo151

Shepard, F.P., Macdonald, G.A. & Cox, D.C. (1950) The Tsunami of April 1, 1946. 5(6), 391–528.

Soloviev, S.L. (1990) Tsunamigenic zones in the Mediterranean Sea. *Natural Hazards*, 3(2), 183–202. Available from: https://doi.org/10.1007/BF00140432

Soloviev, S.L., Solovieva, O.N., Go, C.N., Kim, K.S. & Shchetnikov, N.A. (2000) In: Bonnin, J., Levin, B.W., Tinti, S. & Papadopoulos, G.A. (Eds.) *Tsunamis in the Mediterranean Sea 2000 B.C.–2000 a.D*, Vol. 13. Springer Netherlands. Available from: https://doi.org/10.1007/978-94-015-9510-0

Stiros, S.C. & Papageorgiou, S. (2001) Seismicity of Western Crete and the destruction of the town of Kisamos at AD 365: archaeological evidence. *Journal of Seismology*, 5(3), 381. Available from: https://doi.org/10.1023/A:1011475610236

Sugawara, D., Minoura, K. & Imamura, F. (2020) Tsunamis and tsunami sedimentology. In *Tsunamiites* (2nd Ed.) Delft, Netherlands: Elsevier. Available from: https://doi.org/10.1016/B978-0-12-823939-1.00003-3

Swift, D.J.P. (1968) Coastal erosion and transgressive stratigraphy. *The Journal of Geology*, 76(4), 444–456. Available from: https://doi.org/10.1086/627342

Synolakis, C.E., Bernard, E.N., Titov, V.V., Kânoğlu, U. & González, F.I. (2008) Validation and verification of tsunami numerical models. *Pure and Applied Geophysics*, 165(11–12), 2197–2228. Available from: https://doi.org/10.1007/s00024-004-0427-y

Tang, L., Titov, V.V. & Chamberlin, C.D. (2009) Development, testing, and applications of site-specific tsunami inundation models for real-time forecasting. *Journal of Geophysical Research: Oceans*, 114(C12), 2009JC005476. Available from: https://doi.org/10.1029/2009JC005476

Thalakkottukara, N.T., Thomas, J., Watkins, M.K., Holland, B.C., Oommen, T. & Grover, H. (2024) Suitability of the height above nearest drainage (HAND) model for flood inundation mapping in data-scarce regions: a comparative analysis with hydrodynamic models. *Earth Science Informatics*, 17(3), 1907–1921. Available from: https://doi.org/10.1007/s12145-023-01218-x

The Wamdi Group. (1988) The WAM model—a third Generation Ocean wave prediction model. *Journal of Physical Oceanography*, 18(12), 1775–1810. Available from: https://doi.org/10.1175/1520-0485(1988)018<1775:TWMTGO>2.0.CO;2

Tinti, S. & Maramai, A. (1996) Catalogue of tsunamis generated in Italy and in Côte d'Azur, France: a step towards a unified catalogue of tsunamis in Europe. *Annali di Geofisica*, 39(6), 1253–1268. Available from: https://doi.org/10.4401/ag-4040

Tinti, S., Maramai, A. & Graziani, L. (2004) The new catalogue of Italian tsunamis. *Natural Hazards*, 33(3), 439–465. Available from: https://doi.org/10.1023/B:NHAZ.0000048469.51059.65

Tonielli, R., Innangi, S., Budillon, F., Di Martino, G., Felsani, M., Giardina, F., et al. (2016) Distribution of *Posidonia oceanica* (L.) Delile meadows around Lampedusa Island (strait of Sicily, Italy). *Journal of Maps*, 12(sup1), 249–260. Available from: https://doi.org/10.1080/17445647.2016.1195298

Triantafyllou, I., Agalos, A., Samaras, A.G., Karambas, T.V. & Papadopoulos, G.A. (2024) Strong earthquakes and tsunami potential in the Hellenic subduction zone. *Journal of Geodynamics*, 159, 102021. Available from: https://doi.org/10.1016/j.jog.2024.102021

Van Ormondt, M., Nederhoff, K. & Van Dongeren, A. (2020) Delft dashboard: a quick set-up tool for hydrodynamic models. *Journal of Hydroinformatics*, 22(3), 510–527. Available from: https://doi.org/10.2166/hydro.2020.092

Wang, X. & Power, W.L. (2011) COMCOT: a tsunami generation, propagation and run-up model. In *GNS*.

Warren, I.R. & Bach, H.K. (1992) MIKE 21: a modelling system for estuaries, coastal waters and seas. *Environmental Software*, 7(4), 229–240. Available from: https://doi.org/10.1016/0266-9838(92)90006-P

Yolsal-Çevikbilen, S. & Taymaz, T. (2012) Earthquake source parameters along the Hellenic subduction zone and numerical simulations of historical tsunamis in the eastern Mediterranean. *Tectonophysics*, 536, 61–100. Available from: https://doi.org/10.1016/j.tecto.2012.02.019

How to cite this article: Borzì, L., Scala, P., Distefano, S., Laksono, F.X.A.T., Manno, G., Innangi, S. et al. (2024) Tsunami propagation and flooding maps: An application for the Island of Lampedusa, Sicily Channel, Italy. *Earth Surface Processes and Landforms*, 1–20. Available from: https://doi.org/10.1002/esp.5996